CrossMark

Constraints on oceanic meridional heat transport from combined measurements of oxygen and carbon

L. Resplandy[1] · R. F. Keeling[1] · B. B. Stephens[2] · J. D. Bent[2] · A. Jacobson[3] ·
C. Rödenbeck[4] · S. Khatiwala[5]

Abstract Despite its importance to the climate system, the ocean meridional heat transport is still poorly quantified. We identify a strong link between the northern hemisphere deficit in atmospheric potential oxygen (APO = $O_2 + 1.1 \times CO_2$) and the asymmetry in meridional heat transport between northern and southern hemispheres. The recent aircraft observations from the HIPPO campaign reveal a northern APO deficit in the tropospheric column of -10.4 ± 1.0 per meg, double the value at the surface and more representative of large-scale air–sea fluxes. The global northward ocean heat transport asymmetry necessary to explain the observed APO deficit is about 0.7–1.1 PW, which corresponds to the upper range of estimates from hydrographic sections and atmospheric reanalyses.

✉ L. Resplandy
  lresplandy@ucsd.edu

1 Scripps Institution of Oceanography, University of California San Diego, La Jolla, CA, USA

2 National Center for Atmospheric Research, Boulder, Colorado, USA

3 Earth System Research Laboratory, NOAA, Boulder, Colorado, USA

4 Max Planck Institute for Biogeochemistry, Jena, Germany

5 Department of Earth Sciences, University of Oxford, Oxford OX1 3AN, UK

1 Introduction

Major advances in our understanding of the large scale ocean can be related to the World Ocean Circulation Experiment (WOCE), which was a multi-national ship-based program of unprecedented scale in the 1990s to measure ocean circulation and related transports of heat, salt, carbon, and nutrients. Though great strides were made on many fronts, WOCE did not provide a complete picture of the air–sea fluxes and large scale ocean transports. These needs are still unfilled to this day, despite the advent of the Argo float program and other improvements in sensor oceanography and satellites. The root difficulty is that many elements of the ocean circulation are still too uncertain to infer reliable fluxes and transports.

The ocean gains heat in the tropics and carries it poleward. The ocean heat transport is not symmetric about the equator, however, as the Atlantic overturning circulation transports heat from deep within the Southern Hemisphere to the Northern Hemisphere (Crowley 1992; Marshall et al. 2014; Schneider et al. 2014). This asymmetry in ocean heat transport is a key driver of the climate mean state and variability through its influence on sea surface temperatures. Warmer sea surface temperatures in the north are associated with larger oceanic heat loss to the atmosphere and a major factor causing the displacement of the inter-tropical convergence zone north of the equator (Philander et al. 1996; Fuckar et al. 2013; Marshall et al. 2014; Schneider et al. 2014). The northward meridional heat transport also controls climate variability on decadal to millennial timescales by regulating the sea ice cover in the Arctic and its positive feedback on natural and anthropogenic warming (Crowley 1992; Mahlstein and Knutti 2011). Northward heat transport is also invoked as a major driver of the variability associated with the North Atlantic Oscillation (Bryden et al. 2014).

Estimates of the northward heat transport in the Atlantic range from 0.85 to 1.4 PW (1 Petawatt $= 10^{15}$ W) at approximately 25°N (Hall and Bryden 1982; Macdonald 1998; Bryden and Imawaki 2001; Ganachaud and Wunsch 2003; Talley 2003; Lumpkin and Speer 2007; Trenberth and Caron 2001; Trenberth and Fasullo 2008; Johns et al. 2011). The northward transport in the Atlantic Ocean is partly counterbalanced by a southward transport in other basins resulting in a weaker net meridional transport for the whole ocean. The uncertainties, already significant in the Atlantic basin, increase dramatically when considering the net global transport. A useful measure of the ocean heat transport asymmetry (A_Q) is:

$$A_Q = (T_{20°N} + T_{20°S})/2 \qquad (1)$$

where $T_{20°N}$ and $T_{20°S}$ are the ocean meridional heat transports at 20°N and 20°S either estimated directly from hydrographic sections or computed from steady-state air–sea flux poleward of these latitudes. This metric is effectively an interpolated estimate of the transport across the Equator, but in contrast to estimates of the transport across the Equator is less sensitive to details of the tropical ocean circulation. Estimations from WOCE hydrographic sections (Ganachaud and Wunsch 2003) give a heat transport asymmetry between hemispheres of 0.5 ± 0.6 PW, while indirect methods based on satellite observations and air–sea flux bulk formulations (Large and Yeager 2009) or radiative budgets at the top of the atmosphere (Trenberth and Caron 2001; Fasullo and Trenberth 2008) are spread between 0.1 and 0.8 PW. The long-term global ocean heat warming is of the order of 0.2 PW (Rhein et al. 2013 or 274 ZJ over 40 years). Differences of the order of 0.5 PW between estimates of the heat transport asymmetry are a serious limitation to the understanding of the climate system and its variability.

The relatively weak observational constraint on the global ocean heat transport is matched by similarly large differences between global climate models. Hemispheric ocean heat transport asymmetry (A_Q) in climate models participating in the most recent assessment of the Intergovernemental Panel on Climate Change (IPCC) shows a large spread ranging from slight southward or null transport to intense northward transport larger than 1 PW (see Figure 9.21 in, Flato et al. 2013). Inaccuracy and uncertainties of the order of 0.5–1 PW in the simulated ocean heat transport limits future climate predictions, such as the prediction of El Niño Southern Oscillation and its teleconnections, or shifts in the ITCZ and rainfall associated with climate change (Ham and Kug 2012; Li and Xie 2014).

Here, we show that an additional constraint on the magnitude of the ocean heat transport asymmetry is provided by observations of atmospheric O_2 and CO_2 combined into a tracer called potential oxygen (PO $= O_2 + 1.1 \times CO_2$). Potential oxygen (PO) was first defined in the atmosphere (atmospheric potential oxygen, noted APO) to isolate the oceanic contribution from the land contribution in atmospheric variations of CO_2 and O_2 (Stephens et al. 1998). APO is nearly unchanged by photosynthesis and respiration of land plants because of compensating influences on O_2 and CO_2, which are exchanged in a -O_2:CO_2 ratio of $\sim$ 1.1 (Severinghaus 1995). The primary influences on APO are air–sea exchange of O_2 and CO_2, which are not tightly coupled to each other, and fossil-fuel burning, which have $-O_2$:CO_2 ratios higher than 1.1, depending on the fuel type. Because the fossil-fuel influences are relatively well known, APO measurements can be used to constrain the weighted sum of O_2 and CO_2 fluxes across the air–sea interface.

O_2 and CO_2 air–sea fluxes are driven by changes in solubility, ocean biology and physics. The solubility pump has a similar impact on both gases: when the ocean warms, it releases O_2 and CO_2 to the atmosphere and when it cools it uptakes both. In contrast, the biological pump has opposed effects on O_2 and CO_2. Marine photosynthesis consumes carbon and produces O_2 in surface waters, whereas the respiration of sinking organic matter depletes O_2 and adds carbon to deeper waters. The ocean circulation transports and mixes the gradients set by biological activity, favoring the uptake of O_2 and the release of CO_2 where deep waters re-surface (e.g. winter mixing and upwelling). Sources and sinks of O_2 and CO_2 are coupled within the ocean by the stoichiometry of marine photosynthesis and respiration. Although marine biologically-driven O_2 and CO_2 fluxes are not as closely coupled as land biospheric fluxes, owing to differences in the CO_2 and O_2 equilibration times across the air–sea interface, they do partly cancel. As a result, the thermally driven contributions of O_2 and CO_2 fluxes tend to dominate in terms of their impact on APO at preindustrial times. A close link between APO and heat fluxes is expected because the thermally-induced gas fluxes of O_2 and CO_2 are closely tied to the net air–sea heat flux.

A close link between PO and heat exchange is also expected based on the hydrographic distribution of O_2^* and C^*, which are quasi-conservative ocean tracers that track air–sea exchange of O_2 and CO_2 (Gruber et al. 2001; Gruber and Sarmiento 2002). APO has a mirrored tracer in the ocean, referred to as ocean potential oxygen (OPO $= O_2^*$ + $1.1 \times C^*$) which is conservative with respect to marine biota and whose air–sea fluxes are equivalent to air–sea fluxes of APO. As shown in Fig. 1, the global ocean distribution of oceanic potential oxygen (OPO) is very strongly correlated with potential temperature (slope of -15.6 μmol Kg^{-1} K^{-1}, $r^2 = 0.95$). The gain of OPO by a parcel of water at the
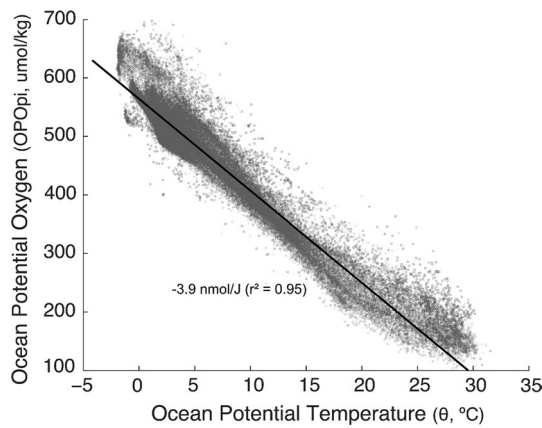
Fig. 1 Ocean potential temperature (θ) versus pre-industrial ocean potential oxygen (OPO_{pi}) in the GLODAP dataset. OPO_{pi} is conservative with respect to the marine biosphere, removes variations associated with anthropogenic carbon using estimates from Khatiwala et al. (2009) and is strongly coupled to thermal air–sea exchanges of O_2 and CO_2. The slope is $-15.6 \, \mu\text{mol} \, Kg^{-1} \, {}^{\circ}C^{-1}$, equivalent to -3.9 nmol per joule of warming as derived by multiplying by an average thermal capacity of $3990 \, J \, Kg^{-1} \, {}^{\circ}C^{-1}$. The curvature in the slope of the data arises from non-linearities in O_2 and CO_2 solubilities, which are more sensitive to temperature change at lower temperature. Note however that this curvature is much smaller for OPO_{pi} than for O_2^* (Gruber et al. 2001; Keeling and Garcia 2002)

air–sea interface has to be associated with a loss of heat. We expect this relationship to also apply to the interhemispheric transport, such that the northward transport of heat should be associated with an uptake of O_2 and CO_2 in the northern hemisphere and a release in the southern hemisphere. A deficit in APO, which reflects the stronger uptake of O_2 and CO_2 has indeed been observed in the Northern Hemisphere (Stephens et al. 1998; Battle et al. 2006; Keeling and Manning 2014) but this observation has not been previously used as a constraint on ocean heat transport.

Here, we present a framework based on oceanic and atmospheric chemical data that is sensitive to the ocean circulation patterns, and can thus be used to challenge models of ocean circulation and their predictions in terms of heat transport. Building up on previous work (Gruber et al. 2001; Jacobson et al. 2007; Mikaloff Fletcher et al. 2007), we use a consistent application of inverse techniques to estimate air–sea fluxes of O_2, CO_2 and heat. We simulate the APO distribution resulting from the inverse air–sea fluxes using an atmospheric transport model and additional fluxes from fossil-fuel burning, seasonal air–sea exchanges, and oceanic uptake of anthropogenic CO_2. To explore the sensitivity of the northern APO deficit to the ocean transport, we used seven different ocean models that differ significantly in their large-scale circulation and transport. Simulated APO deficits in the Northern Hemisphere are
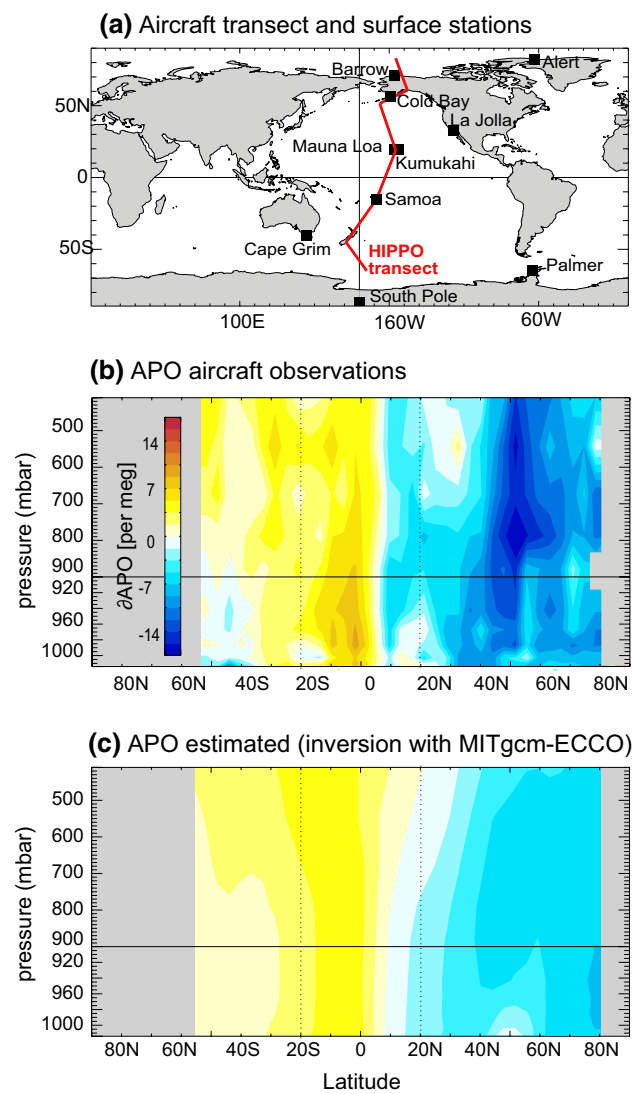

Fig. 2 a Map of the approximate transect of HIPPO aircraft campaigns (*red line*) and position of the 9 atmospheric Scripps surface stations (*black symbols*). **b, c** Annual mean meridional APO gradient and referenced to the value at Cape Grim station (∂APO = APO–APO (Cape Grim), in per meg): **b** observed during the HIPPO aircraft campaign and **c** estimated along the HIPPO transect from inverse air–sea flux estimates using GLODAP data, MITgcm-ECCO ocean transport and TM3 atmospheric transport

then evaluated against recent observations from the High-Performance Instrumented Airborne Platform for Environmental Research (HIAPER) Pole-to-Pole Observations (HIPPO) large-scale aircraft campaign (Wofsy 2011).

We find a northward heat transport in the upper range of previous estimates is necessary to explain the observed APO deficit. We also show that column-average aircraft observations provide superior constraints on large-scale oceanic fluxes than surface data.

2 Methods

2.1 Atmospheric observations

This study takes advantage of the recent airborne HIPPO campaign (Wofsy 2011). The APO dataset relies on a combination of flask and in situ CO_2 concentrations and O_2/N_2 ratios sampled along a meridional transect in the Pacific (Fig. 2). The HIPPO data resolve the vertical distribution of APO over the troposphere based on 7 mid-Pacific transects covering the seasonal cycle between 2009 and 2011.

APO (in per meg) is calculated from measurements of CO_2 concentrations and O_2/N_2 ratios (Stephens et al. 1998) according to:

$$APO \quad [\text{per meg}] = \delta(O_2/N_2) + \frac{1.1}{X_{O2}} * (CO_2 - 350 \quad [\text{ppm}]) \tag{2}$$

with

$$\delta(O_2/N_2) \quad [\text{per meg}] = \left[\frac{(O_2/N_2)_{sample}}{(O_2/N_2)_{reference}} - 1 \right] * 10^6 \tag{3}$$

where $\delta(O_2/N_2)$ is in per meg, CO_2 in ppm (i.e. μmol. mol^{-1}), 1.1 is the approximate ratio of O_2 production to CO_2 consumption in terrestrial carbon storage (Severinghaus 1995), X_{O2} is the atmospheric mole fraction of O_2 necessary to convert $[CO_2]$ from ppm to per meg units ($X_{O2} = 0.2094$), and 350 is an arbitrary reference for CO_2.

Here we focus on the northern APO deficit, which we quantify in two different ways: 1) the difference between the meridionally integrated APO content north of 20°N (20°N-80°N) and south of 20°S (58°S–20°S) from 900 mb HIPPO data (noted ΔAPO 900mb) and 2) the same as 1) but column-averaged over the troposphere up to 400 mb (noted ΔAPO column). Further details on APO sampling, uncertainties and spatio-temporal interpolation used to derive annual mean values are presented in "Appendix 1".

2.2 Ocean observations

We use ocean interior data from the GLobal Ocean Data Analysis Project (GLODAP) version 1 (Key et al. 2004). Conservative tracers related to air–sea fluxes C^* and O_2^* are computed following (Gruber et al. 2001; Gruber and Sarmiento 2002).

$$C^* = DIC - \Delta DIC_{Bio}$$
$$= DIC - R_{C:P}PO_4 - 1/2(Alk + R_{N:P}PO_4) \tag{4}$$

$$O_2^* = O_2 - \Delta O_{2Bio}$$
$$= O_2 - R_{O:P}PO_4 \tag{5}$$

All concentrations including DIC, phosphate (PO_4) and alkalinity (Alk) are salinity normalized to account for dilution changes. $R_{N:P} = 170$, $R_{C:P} = 16$ and $R_{O:P} = -170$ are the elemental ratios we use for the conservation of C^* and O_2^* with respect to marine photosynthesis (Anderson and Sarmiento 1994). We compute the pre-industrial component of C^* used in our ocean inversion as follows:

$$C_{pi}^* = C^* - C_{anth} \tag{6}$$

where C_{anth} is the anthropogenic component of dissolved inorganic carbon from Khatiwala et al. (2009, 2013). This subtraction is done at each observational point. Pre-industrial oceanic potential oxygen (OPO_{pi}) is then computed as:

$$OPO_{pi} = O_2^* + 1.1 \times C_{pi}^* \tag{7}$$

Dissolved N_2 concentrations are computed following Hamme and Emerson (2004) using GLODAP temperature and salinity (see details in "Appendix 2").

2.3 Ocean interior inversion and potential oxygen air–sea flux

We compute global distributions of air–sea fluxes using the ocean inversion technique of Gloor et al. (2001); Gruber et al. 2001) and Mikaloff Fletcher et al. (2007), which yields steady-state fluxes based on ocean interior data and modeled ocean transport. The choice of the inversion technique is motivated by its ability to get observation-based estimates of all air–sea fluxes (CO_{2pi}, O_2, N_2 and heat) in a consistent framework. Our application of the inverse method is limited to deriving steady-state pre-industrial fluxes. We assume that O_2, N_2 and heat contemporary fluxes are similar to the pre-industrial fluxes and therefore can be computed directly from O_2^*, N_2 solubility and potential temperature respectively. For example, changes in atmospheric O_2 concentration due to anthropogenic activities (fossil fuel burning and land use) are estimated to be less than 0.1 % (Keeling and Manning 2014), while changes in oceanic O_2 concentrations due to climate change are of the order of ∼ 40 T mol year^{-1} (Keeling et al. 2010), which represents less than 0.1 % of the O_2 content in surface waters (<100 m). The inverse calculation for CO_2 is done exclusively on the C_{pi}^* component, thus deriving an estimate of the pre-industrial air–sea CO_2 flux. Ocean interior inversions incorrectly interpret the addition of carbon by rivers as an air-to-sea flux (see discussion in Gruber et al. (2009) supplementary material). Here we do not correct for rivers as we focus on ocean meridional transports, which implicitly include the contributions of air–sea and river fluxes. Further details on the ocean inversion and its uncertainties are presented in "Appendix 2".

Table 1 Overturning circulation following Gnanadesikan (1999)

	MOM-HH	MOM-LHS	MOM-LL	MOM-PSS	MOM-RDS	MITgcm-2.8	MITgcm-ECCO
M_{North}	15.3	15.9	14.5	16.1	16.2	15.5	20.5
M_{South}	−8.4	4.9	3.9	11.3	2.7	2.3	12.6
$M_{Upwelling}$	23.8	11	10.6	4.8	13.5	13.2	7.9

Units are Sv. M_{North} is the maximum northward transport at 48°N using the meridional stream function. M_{South} is the transport across the thermocline ($\sigma_\theta = 24.7$) at 32°S. The contribution of $M_{Upwelling}$ is then deduced from the difference between M_N and M_{South}

2.4 Ocean transport models

We carry out the ocean inversion calculation using ocean transports from seven different ocean models that differ significantly in their large scale circulation. Five of the ocean models used in the inversion are from the MOM suite (Jacobson et al. 2007) and two are MITgcm models (Marshall et al. 1997). The MOM suite (Table 1) was designed to explore the impact of a wide range of transports that reproduced the observed density distribution in the ocean (e.g., Gnanadesikan et al. 2002; Palter et al. 2010). It includes MOM-HH (high diapycnal and eddy diffusivity), MOM-LHS (low diapycnal diffusivity and high eddy diffusivity in Southern Ocean), MOM-LL (low diapycnal and eddy diffusivity), MOM-PSS (sometimes referred as P2A, low diapycnal diffusivity, high eddy diffusivity in Southern Ocean, narrow Drake Passage) and MOM-RDS (sometimes referred as P2, low diapycnal diffusivity, high eddy diffusivity in Southern Ocean, salinity restoring), all on a coarse resolution grid of 4° × 5°. The two MITgcm models provide further insight on the sensitivity to ocean transport, with the coarse resolution model (2.8°, denoted MITgcm-2.8) and the 1° × 1° ECCO version 3 ocean state estimate (denoted MITgcm-ECCO) that assimilates numerous satellite and in-situ observations (Wunsch et al. 2009).

To quantify the differences in large-scale ocean circulation between the seven models, we used the scheme of Gnanadesikan (1999), which divides the deep meridional overturning circulation (MOC) into three components: (1) dense water formation and sinking in the North Atlantic (M_{North}), (2) upwelling of deep waters in the thermocline due to the downward mixing of heat transforming dense waters into lighter waters ($M_{Upwelling}$) and (3) the net conversion of deep to thermocline water in the Southern Ocean (M_{South}), reflecting the balance between Ekman and eddy components (Fig. 3; Table 1).

All the OGCMs used here have rates of dense water formation in the North Atlantic of about 15–20 Sv (1 Sverdrup (Sv) = 10^6 m³), in agreement with observation-based estimates (Talley 2008; Lumpkin and Speer 2007).
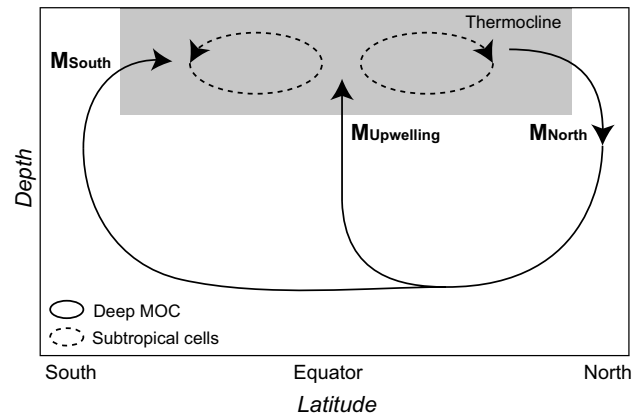

Fig. 3 a Schematic of the meridional circulation associated with (1) the deep meridional overturning circulation (MOC) that transforms thermocline waters into deep waters and vice-versa and (2) the shallow circulation within the thermocline e.g. the subtropical cells. The main fluxes of the deep MOC described by Gnanadesikan (1999) are shown: the northern sinking flux (M_{North}), the upwelling of deep waters in the tropical region ($M_{Upwelling}$) and the balance between wind-driven upwelling and eddy-return flow in the Southern Ocean (M_{South}). Note that $M_{North} = M_{South} + M_{Upwelling}$

Their circulations differ mainly by the relative contribution of the tropical upwelling and the wind-driven transport in the Southern Ocean in returning deep waters to the surface (Table 1). MOM-HH, MOM-RDS and MITgcm-2.8 are dominated by the deep tropical upwelling (>13 Sv). In the extreme case of MOM-HH, the tropical upwelling even surpasses the North Atlantic deep water formation (~24 Sv) and leads to a southward flow in the Southern Ocean (M_{South} = −8.4 Sv). In contrast, MOM-PSS and MITgcm-ECCO are characterized by strong northward wind-driven flow in the Southern Ocean (~12 Sv) and weak tropical upwelling (<8 Sv). Finally, MOM-LL and MOM-LHS lie somewhere in between, with a relatively strong contribution of the tropical upwelling (~11 Sv) and a significant wind-driven flow from the south (~4 Sv). Refer to "Appendix 2" for a description of the ocean models and how this study differs from previous studies.

2.5 Atmospheric transport modelling

We used the 3-D Eulerian atmospheric transport model (ATM) Tracer Model version 3 (TM3, Heimann and Körner 2003) to simulate annual mean APO distributions using inverse O_2 and CO_{2pi} air–sea fluxes combined with several different components: (1) N_2 fluxes also from the same inversions; (2) air–sea fluxes of anthropogenic CO_2 from Khatiwala et al. (2009), (3) uptake of O_2 and CO_2 from fossil fuel burning from the Emission Database for Global Atmsopheric Research (EDGAR, available at http://edgar.jrc.ec.europa.eu); and (4) seasonal O_2, CO_2 and N_2 components from Garcia and Keeling (2001), Rödenbeck et al. (2013) and based on solubility changes expected form the seasonality in heat fluxes (Keeling and Shertz 1992) respectively. N_2 fluxes are relevant to derive APO as they modify the O_2/N_2 ratio measured in the atmosphere (Eqs. 2 and 3). The seasonal components are relevant because of the so-called rectifier effect, in which interactions between seasonal variations in atmospheric transport and seasonal surface fluxes influence the annual mean. Further details on APO simulation and uncertainties from the different source components can be found in "Appendix 3".

The TM3 model carries excesses or deficits in O_2, N_2 and CO_2 as if all three were trace gases in $\mu\mu$mol mol^{-1} (ppm) units. To allow comparison to observations, changes in APO in per meg units are computed following Stephens et al. (1998):

$$\Delta APO = \frac{\partial APO}{\partial O_2} \times \Delta O_2 + \frac{\partial APO}{\partial N_2} \times \Delta N_2 + \frac{\partial APO}{\partial CO_2} \times \Delta CO_2$$
$$= \frac{1}{X_{O2}} \times \Delta O_2 - \frac{1}{X_{N2}} \times \Delta N_2 + \frac{1.1}{X_{O2}} \times \Delta CO_2 \quad (8)$$

where ΔO_2, ΔN_2 and ΔCO_2 are the changes in ppm and X_{O2} and X_{N2} the atmospheric mole fractions of O_2 and N_2 ($X_{O2} = 0.2094$ and $X_{N2} = 0.7808$).

TM3 was run at a horizontal resolution of 4° latitude by 5° longitude with 19 vertical levels and driven by 6-h meteorological fields derived from reanalyses between 1990 and 2013. To explore sensitivity to atmospheric circulation, winds from two reanalyses were used: NCEP (Kalnay et al. 1996) and ERA-Interim (Dee et al. 2011). Annual mean values of ΔO_2, ΔN_2, and ΔCO_2 were computed from the last 10 years (1994–2013). The northern APO deficit was computed following the same approach as in observations (see Sect. 2.1). Uncertainties in the atmospheric transport were evaluated by comparing results obtained with TM3 and with another transport model (the Center for Climate System Research/National Institute for Environmental Studies/Frontier Research Center for Global Change model, CCSR/NIES/FRCGC (Miyazaki et al. 2008)) when run with a common set of APO fluxes.

3 Results

3.1 General features of diagnosed air–sea fluxes

3.1.1 O_2, N_2 and pre-industrial CO_2 fluxes

The O_2, N_2 and CO_{2pi} air–sea fluxes obtained from the inverse calculations are in qualitative agreement with the previous results of Gruber et al. (2001), Mikaloff Fletcher et al. (2007) and Gerber and Joos (2010) (Fig. 4). The tropical band is the major outgassing region of CO_{2pi}, O_2 and N_2. The ocean at mid-latitude and high latitude in the northern hemisphere is on average a sink for the 3 gases. In contrast, CO_{2pi} fluxes in the southern hemisphere are generally opposed to O_2 and N_2 fluxes, with the ocean being a large sink of CO_{2pi} and a source of O_2 at mid-latitude and a source of CO_{2pi} and a sink of O_2 and N_2 at high latitude.

Two features that are quite sensitive to the ocean transports are the strength of the tropical outgassing and the balance between southern mid-latitudes and southern high-latitudes (Fig. 4). For example in the tropical band, the outgassing of O_2 is about 30 % stronger in the inverse calculation with MOM-HH than with MITgcm-ECCO. At southern mid-latitudes, the outgassing of O_2 varies by a factor larger than 10 between MOM-RDS and MOM-PSS. Another sensitive feature is the distribution of the northern hemisphere ingassing of O_2 and N_2 between mid-latitudes and high-latitudes. This mostly arises from the differences in the representation of the North Atlantic winter mixing, which is more concentrated north of 49°N in the MITgcm runs than in the MOM-suite runs.

CO_{2pi} air–sea fluxes computed here are similar to the previously published runs (Mikaloff Fletcher et al. 2007; Gerber and Joos 2010) but there are significant differences between O_2 and N_2 fluxes and those published in Gruber et al. (2001). In particular, the ocean uptake in the northern hemisphere is mostly located at mid-latitude in Gruber et al. (2001), while it is at higher latitude in our estimate (Fig. 4). This difference is related to the lower resolution of the inversion used in Gruber et al. (2001) (13 vs. 21 regions, Table 6).

3.1.2 Relation between heat and pre-industrial potential oxygen air–sea fluxes

The flux of pre-industrial potential oxygen across the air–sea interface is computed from the combination of O_2 and CO_{2pi} inverse fluxes:

$$F_{POpi} = F_{Oan} + F_{Cpi} \quad (9)$$

where F_{Oan} and F_{Cpi} are the annual mean air–sea fluxes of oxygen and pre-industrial carbon obtained for each ocean
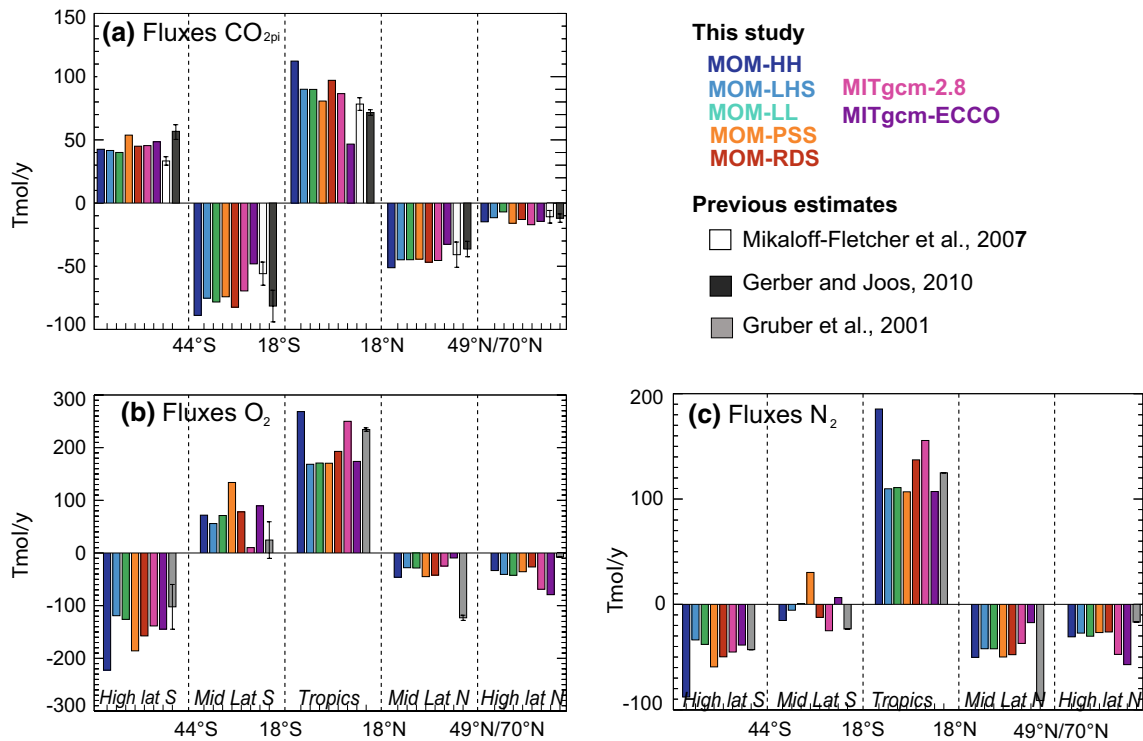
Fig. 4 Air–sea fluxes based on ocean interior inversions for **a** pre-industrial CO_2, **b** O_2 and **c** N_2. The results obtained with the 7 OGCMs in this study (*color*) are compared to previous estimates (mean $\pm$ 1 standard deviation across obtained estimates): Mikaloff

Fletcher et al. (2007, 10 estimates) and Gerber and Joos (2010, 4 estimates) for CO_{2pi} and Gruber et al. (2001, 2 estimates) for O_2 and N_2. Note that the northern high-latitude region is north of 49°N in the Pacific and north of 70°N in the Atlantic

inversion. We find that the PO_{pi} air–sea flux is strongly anti-correlated by zone to the air–sea heat flux (Figs. 5, 6). This relationship is insensitive to the ocean model with an ocean loss of about 120 Tmol year^{-1} of PO_{pi} for a heat uptake of 1 PW and *vice versa*, which is equivalent to a slope of -3.8 nmol J^{-1} similar to the strong correlation between OPO_{pi} and potential temperature noted earlier (slope of -3.9 nmol J^{-1} on Fig. 1).

The large-scale anti-correlation between heat and PO_{pi} fluxes is reflected in the opposed hemispheric asymmetry in heat and PO_{pi} ocean transport (defined as the average of the fluxes across 20°N and 20°S, see Eq. 1, Fig. 6). All models except MOM-HH show a net northward heat transport asymmetry, with a magnitude that is closely tied to the southward PO_{pi} flux (Fig. 6).

3.2 Observational constraints on ocean meridional heat transport

Figure 7 compares the ocean heat transports derived from the inverse calculations against estimates based on hydrographic sections by Macdonald (1998), Ganachaud and Wunsch (2003), Talley (2003) and Johns et al. (2011). In the Atlantic, our inverse estimates are generally weaker,
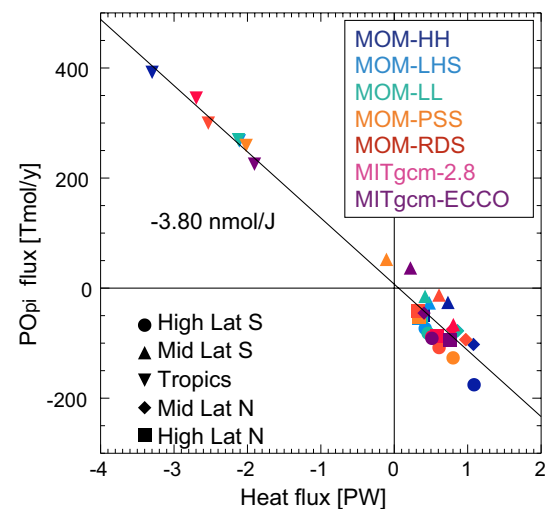

Fig. 5 Air–sea pre-industrial potential oxygen (PO_{pi}) flux versus air–sea heat flux obtained from the 7 inverse estimates and for the latitudinal bands of Fig. 6 **a**, **d**

in particular at low latitude where they underestimate the observationally estimated transport by $\sim$0.2–0.6 PW (Fig. 7b). In the North Pacific, estimates from two
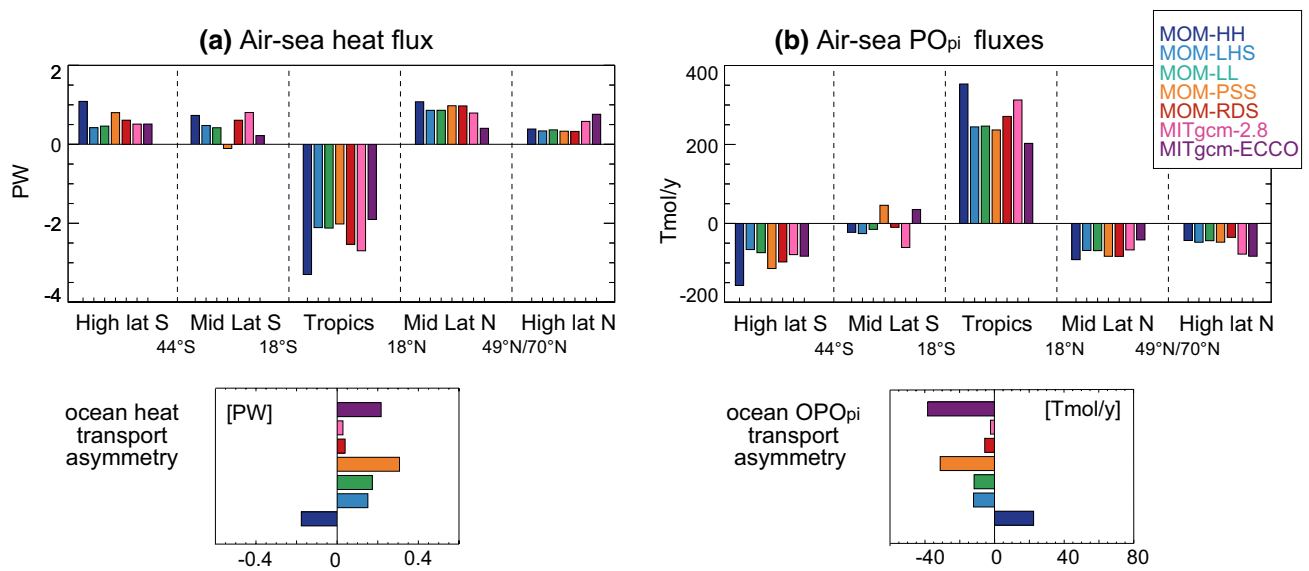
Fig. 6 Air–sea fluxes and interhemispheric transports of **a** heat and **b** pre-industrial PO (PO$_{pi}$). APO$_{pi}$ fluxes are based on the 7 ocean interior inversion results shown in Fig. 4. The associated oceanic inter-hemispheric transports of heat and pre-industrial OPO (OPO$_{pi}$) are computed as the asymmetry between 20°S and 20°N
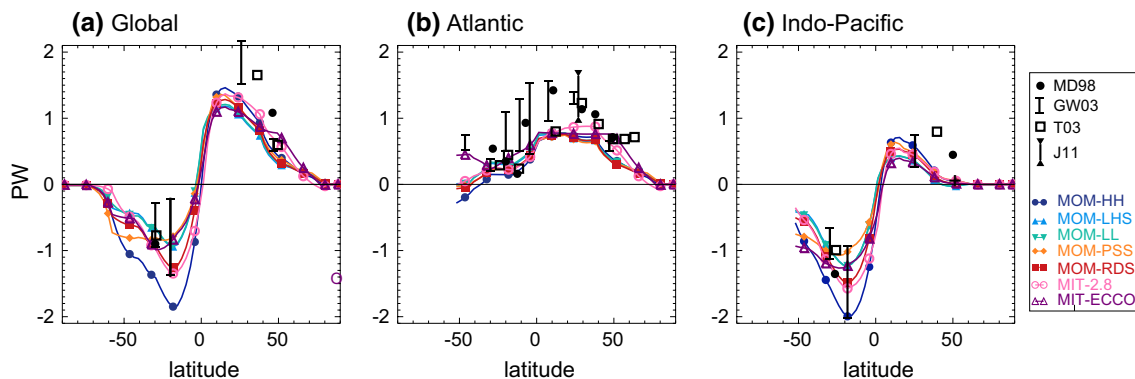

Fig. 7 Oceanic meridional heat transport in **a** the global ocean, **b** the Atlantic and **c** the Indo-Pacific. Transports are positive northward. Units are PW. Observations are from Macdonald (1998, MD98), Tal-ley (2003, T03), Ganachaud and Wunsch (2003, GW03) and Johns et al. (2011, J11)

hydrographic sections suggest that inverse results underestimate the northward transport between 35°N and 50°N, the latitudes of the Kuroshio Current (Fig. 7c). As a result, the northward transport in the Northern Hemisphere at global scale is underestimated by at least 0.2 PW and possibly by as much as 1 PW (Fig. 7a).

In the Southern Hemisphere, the large spread in the southward heat transport at 10°S–50°S (−2 PW to −1 PW) is dominated by the Indo-Pacific (Fig. 7a, c). Transports from hydrographic sections are in the weaker end or lower than the transports obtained from the inverse computation

and exclude the estimate of MOM-HH, which is characterized by strong southward heat transport and a southward return flow in the Southern Hemisphere (Table 1). We find that inverse solutions best reproducing observationally estimated heat transport in the Southern Hemisphere are based on models with stronger wind-driven upwelling in the Southern Ocean (M$_{South}$) and weaker tropical upwelling (M$_{Upwelling}$, in Table 1). However, only three sections associated with large uncertainties are available in the southern Indo-Pacific, which prevents us from constraining further the heat transport at the global scale.

Table 2 ΔAPO column along the HIPPO transect in the data and from ocean inversions, the contributions of fossil fuel (ff), seasonal rectifier effect (seas) and anthropogenic carbon (C_{anth}) used in all inversions, and the contributions of annual mean O_2 (O_{an}), Cpi (C_{pi}) and N_2 (N_{an}) from the MITgcm-ECCO inversion

	ΔAPO column
HIPPO	-10.4 ± 0.9
MOM-HH	-3.9 ± 0.8
MOM-LHS	-5.9 ± 0.8
MOM-LL	-6.0 ± 0.8
MOM-PSS	-6.0 ± 0.8
MOM-RDS	-5.2 ± 0.8
MITgcm-2.8	-5.0 ± 0.8
MITgcm-ECCO	-6.4 ± 0.8
ff	-6.6 ± 0.01
seas	-0.9 ± 0.2
C_{anth}	3.4 ± 0.1
MITgcm-ECCO C_{pi}	-2.4
MITgcm-ECCO O	<-0.1
MITgcm-ECCO N	0.2

3.3 Observed and modeled APO gradients

Observations along the HIPPO transect show an APO deficit of 5–20 per meg in the northern hemisphere, first noted by Stephens et al. (1998) and an APO excess of 5–10 per meg near the equator in the Southern hemisphere, referred to as the equatorial bulge in previous studies (Fig. 2b, Stephens et al. 1998; Battle et al. 2006; Tohjima et al. 2005, 2012). We computed APO gradients from inverse annual mean O_2, CO_{2pi} and N_2 fluxes, combined with the additional components due to the seasonal rectifier effect for all three gases, the anthropogenic carbon air–sea flux and fossil fuel burning. Although MITgcm-ECCO air–sea fluxes

give the strongest north-south asymmetry in APO, it is still unable to reproduce the amplitude of the asymmetry captured in aircraft data (Fig. 2b, c).

Figure 8 shows model results for the total APO gradient and its components at the surface and averaged over the atmospheric column. The wind product (NCEP vs. ERA-Interim) has only a weak impact on the latitudinal gradient obtained on these large spatial and temporal scales (Fig. 8a). Fossil fuel burning and anthropogenic carbon components oppose each other and together produce only a small contribution to the north-south gradient at the surface and in average over the column (Fig. 8b, c). Note that the contributions of fossil fuel and anthropogenic carbon are also relatively well known and therefore introduce little uncertainty in the modeled APO gradient (Table 2).

The seasonal rectifier effect mostly increases annual mean surface APO values at mid- and high-latitudes and produces a deficit at low latitudes (Fig. 8b), because vertical mixing over the ocean is weak in summer when O_2 is outgassing and strong in winter when O_2 is ingassing. According to the atmospheric transport model used here (TM3), the excess due to the rectifier effect at the surface is larger in the north than in the south, so that the rectifier contributes to reduce the surface northern deficit arising from the other components. This effect has been shown to be sensitive to the transport model used (Stephens et al. 1998; Blaine 2005; Battle et al. 2006). Column averages are, however, less sensitive to the rectifier (Fig. 8c), due to compensation of high rectifier values at the surface, where summer trapping of APO occurs, and lower values aloft (Fig. 9). As a result, the uncertainty related to the rectifier effect is relatively small when considering column-averaged APO values (Table 2). In addition to lower rectifier uncertainties, column-averaged values are more representative of annual large-scale air–sea fluxes as they integrate local air–sea fluxes, mostly captured at the surface, and
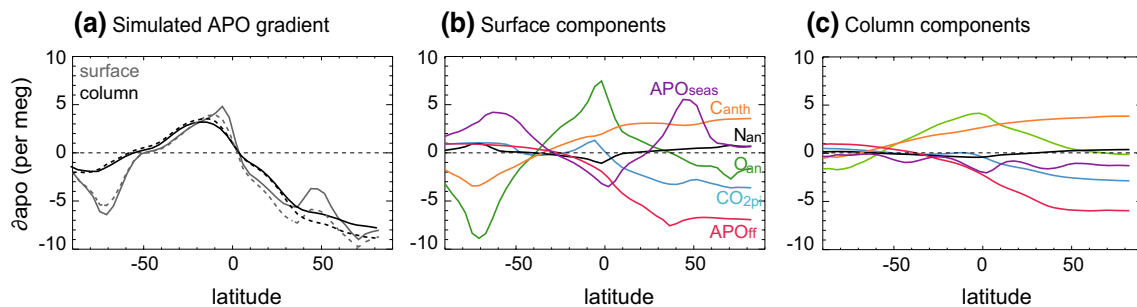
Fig. 8 a APO obtained by transporting MITgcm-ECCO air–sea fluxes with TM3: **a** Surface and column-average APO gradient in the Pacific (180 W) using NCEP winds (*solid lines*) or ERA-Interim winds (*dashed lines*). Contributions to the total APO **b** at the surface and **c** column-averaged from: the seasonally varying or rectifier effect including O_2, CO_2 and N_2 components (APOseas), the anthropogenic carbon air–sea flux (Canth), the fossil fuel combustion (APOff) and the pre-industrial steady state components from O_2 (O_{2an}), CO_2 (CO_{2pi}) and N_2 (N_{2an}). All values are referenced to the value at the Cape Grim station (41°S)

Fig. 9 Contribution of the rectifier effect to the annual mean meridional APO gradient in the Pacific as predicted by TM3 and referenced to the value at Cape Grim station (∂APO = APO-APO(Cape Grim), in per meg)
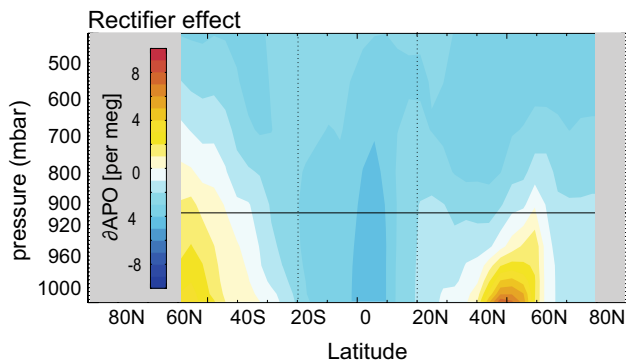
remote air–sea fluxes, captured aloft after being mixed vertically and transported horizontally in the troposphere (Figs. 2b, c, 8).

3.4 Model/data comparison of northern APO deficit

The two different metrics of the northern APO deficit (900 mb and column averaged) are compared against each other and against the heat transport asymmetry in Fig. 10. At the surface (900 mb) the observed APO northern deficit is −5.7 ± 1.5 per meg (Fig. 10a, see method detail in section 2.1). The column-averaged deficit is about 4 per meg larger than the gradient at 900 mb (−10.4 ± 0.9 per meg, Fig. 10a, b). The column gradient is strengthened by the notably low APO values observed in the mid-troposphere between 40°N and 60°N (Fig. 2b). Individual HIPPO transects show that this mid-tropospheric deficit in APO is strongly influenced by a deficit in $\delta(O_2/N_2)$ in the northern hemisphere during winter.

Simulations using MITgcm-ECCO, MOM-PSS, MOM-LHS and MOM-LL succeed at reproducing the northern APO deficit at the surface within the error bars (Fig. 10a). Simulations based on other ocean models mostly represent smaller northern APO deficits. In contrast, all models fail at capturing the vertically integrated northern APO deficit (Fig. 10b; Table 2). MITgcm-ECCO, as well as the other models, also underestimate the mid-tropospheric APO minimum in the north as can be seen by comparing Fig. 2b, c. The extent of this underestimation varies, with MITgcm-ECCO, MOM-PSS, MOM-LHS and MOM-LL reproducing about 65 %, MOM-RDS and MITgcm-2.8 about 50 % and MOM-HH only 40 % of the observed northern deficit (Table 2).

Figure 10b shows that the magnitude of the northern APO deficit is strongly correlated with the heat transport
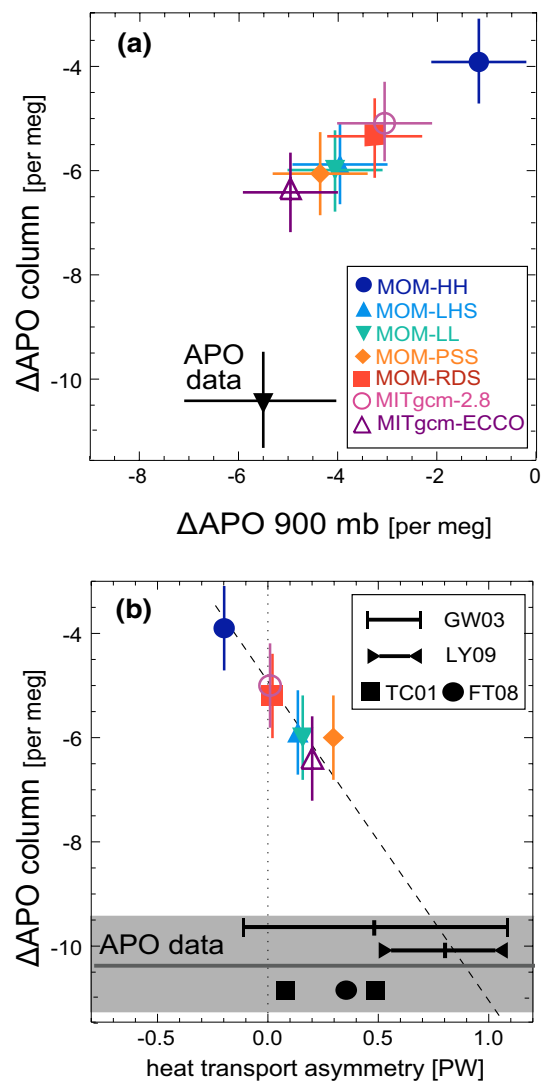

Fig. 10 a Evaluation of the northern atmospheric potential oxygen (APO) deficit using the airborne HIPPO transect at 900 mb (ΔAPO 900 mb) and column averaged over the lower troposphere (ΔAPO column). **b** Relationship between ΔAPO column and the meridional heat transport. The HIPPO observation and uncertainty are shown by a *horizontal gray line* and *lighter gray shading*. Meridional heat transports from hydrographic sections (Ganachaud and Wunsch 2003, GW03), air–sea fluxes bulk formulations (Large and Yeager 2009, LY09) and *top* of the atmosphere budgets (Trenberth and Caron 2001; Fasullo and Trenberth 2008 TC01 and FT08) are indicated in *black* (see details in Table 3)

asymmetry across models, with stronger northern deficits, associated with stronger northern heat transport. If we extrapolate based on this correlation, the underestimation of the APO deficit by ∼3 per meg in MITgcm-ECCO corresponds to an underestimation of the northward ocean heat transport of ∼0.5–0.6 PW globally (Fig. 10b). The global meridional heat transport needed to explain the observed APO deficit is 0.7–1.1 PW (found as the intersection of the

model fit line and the HIPPO observation including uncertainties), which is in the upper range of the Ganachaud and Wunsch (2003) estimate based on hydrographic sections and in agreement with the estimate of Large and Yeager (2009) based on air–sea fluxes bulk formulations (Fig. 10b).

4 Discussion

4.1 Northern APO deficit supports strong ocean heat transport asymmetry

The hemispheric asymmetry in APO observed in the atmosphere demands a larger oceanic uptake of potential oxygen (PO) in the northern hemisphere and a southward transport of OPO in the ocean to maintain the asymmetry. We used inverse methods based on ocean observations and seven models of ocean circulation to compute air–sea fluxes of O_2, CO_2, N_2 and heat and their associated heat transport. We showed that PO and heat are tightly coupled via air–sea fluxes and ocean transport (slope of 3.9 ± 2 nmol J^{-1}). Using an atmospheric transport model, we obtained the atmospheric APO distribution expected from the seven air–sea flux simulations. Four of them, namely those using MITgcm-ECCO, MOM-PSS, MOM-LHS and MOM-LL oceanic transports, reproduce the north-south APO gradient observed at 900 mb within the error bars (-5.7 ± 1.5 per meg). We compared this estimate with the northern APO deficit obtained from 20-year long surface stations data (-4.5 ± 1.5 per meg, see supplementary material Fig S2). The agreement between the two metrics, which are derived from different spatio-temporal coverage and different sampling techniques, shows that the gradient is quite well resolved by aircraft observations.

The comparison at the surface is hampered, however, by uncertainties on the impact of seasonal fluxes on the annual mean, via the so-called rectifier effect (Stephens et al. 1998; Battle et al. 2006; Gruber et al. 2001). A major achievement of this study relies on the extensive sampling effort deployed during the 2009–2011 HIPPO aircraft campaign. This dataset shows that the northern APO deficit in the mid-troposphere is almost two times larger than in the TM3 atmospheric transport simulations at the surface (-10.4 ± 0.9 per meg). These HIPPO observations reveal that although some of the estimates reproduce the northern APO deficit at the surface, they fail to reproduce the column-averaged gradient (Fig. 10). The column-averaged annual gradient integrates the signal of local air–sea fluxes trapped in the seasonally-varying boundary layer as well as remote air–sea fluxes mixed by dominant meridional winds, and is therefore more representative

of the large-scale global air–sea fluxes. Among the ocean transport schemes, MITgcm-ECCO yields a northern deficit with the least disagreement with the observations, which could be expected as the MITgcm-ECCO model is a state of the art ocean state estimate that represents the circulation at higher resolution and assimilates satellite and in-situ data. Nevertheless the improvement of using MITgcm-ECCO is relatively small compared to three of the MOM inversions (MOM-PSS, MOM-LHS and MOM-LL) that predict very similar large-scale patterns and APO deficit, although they are based on ocean models at much lower resolution.

Failure to capture the column averaged northern APO deficit suggests that inverse solutions mis-represent the north-south asymmetries in annual mean potential oxygen fluxes. In reality, there is more potential oxygen uptake in the northern hemisphere and more release in the south than found in any of the inverse calculations. By this logic, the agreement with some of the models at 900 mb (Fig. 10a) must partly be spurious, as a result of compensating errors in the surface fluxes and in atmospheric transport, possibly related to the rectifier effect. This is possible if the rectifier, particularly in the Northern Hemisphere, is underestimated by the TM3 simulations of atmospheric transport. In summer, the ocean poleward of 40° in both hemispheres is a source of potential oxygen and the atmospheric planetary boundary layer is shallow (Stephens et al. 1998; Nevison et al. 2008). The rectifier effect creates an annual mean APO excess near the surface at mid- and high-latitudes. We find that this excess is however larger in the north than in the south, probably because of continental masses reinforcing seasonal mixing differences in the north. A too weak rectifier effect would therefore artificially strengthen the surface northern deficit and explain the spurious agreement at the surface. The HIPPO data effectively back this point, by showing a considerably larger gradient in the mid troposphere than at the surface. This highlights the added value of airborne observations sampling the full troposphere over surface-only measurements.

Although all simulations, regardless of ocean circulation model, systematically underestimate the northern APO deficit, they show a robust relationship between the deficit and the ocean heat transport asymmetry. Based on this relationship, the hemispheric ocean heat transport asymmetry necessary to explain the observed northern APO deficit is about 0.7–1.1 PW. This estimate is in agreement with the most recent estimate based on air–sea flux bulk formulations (Large and Yeager 2009), falls in the upper range of transports derived from hydrographic sections (Ganachaud and Wunsch 2003) and is larger than top of the atmosphere budgets (Trenberth and Caron 2001; Fasullo and Trenberth 2008) (Table 3).

Table 3 Global ocean heat transport asymmetry between 20°S and 20°N (in PW) from hydrographic sections (Ganachaud and Wunsch 2003; Talley 2003), air–sea flux bulk formulations (Large and Yeager 2009) and top of the atmosphere budgets (Trenberth and Caron 2001; Fasullo and Trenberth 2008), the MITgcm-ECCO forward simulation and our inverse calculation based on the same version of MITgcm-ECCO. Note that meridional heat transports are computed where sections are available in observations: between 24°S and 24°N for Talley (2003) and between 19°S and 24°N for Ganachaud and Wunsch (2003)

Estimates	Global	Atlantic	Indo-Pacific
This study	0.7–1.1	–	–
Ganachaud and Wunsch (2003)	0.5 ± 0.6	1 ± 0.3	0.5 ± 0.5
Talley (2003)	–	0.8	–
Large and Yeager (2009)	0.8 ± 0.3	–	–
Fasullo and Trenberth (2008)	0.4	–	–
Trenberth and Caron (2001) ECMWF	0.1	–	–
Trenberth and Caron (2001) NCEP	0.5	–	–
MITgcm-ECCO forward	0.3	0.6	−0.3
MITgcm-ECCO inverse (this study)	0.2	0.5	−0.3

Table 4 Mean and interannual variability (± 1 standard deviation) of the northward heat transport (in PW) at 26°N in the Atlantic Ocean. Results from the MITgcm-ECCO forward simulation are compared to observations from the RAPID array and the Florida Straight survey (Johns et al. 2008, 2011). The total meridional heat transport across the section ($\iint_{xz} \rho c_p \times v \times \theta dxdz$) is broken down into the contributions of overturning ($\int_z \rho c_p \times \bar{v} \times \bar{\theta} dz$) and gyre circulation ($\iint_{xz} \rho c_p \times v^* \times \theta^* dxdz$)

	Observations	MITgcm-ECCO
Total	1.33 ± 0.40	1.08 ± 0.21
Gyre	-0.15 ± 0.07	-0.05 ± 0.05
Overturning	1.18 ± 0.37	1.03 ± 0.23

v is the meridional velocity and θ the potential temperature. Overbars denote the zonal average across the entire transoceanic section and asteriks the deviations from this mean (Johns et al. 2011)

4.2 Missing APO sink/heat source in Northern Hemisphere

HIPPO seasonal data suggest that the underestimation of the northern deficit and the mid-tropospheric drop in APO in our inverse results is associated with a too weak oceanic uptake of oxygen during winter in the northern hemisphere. Two oceanic regions could trigger a strong winter APO decrease in the northern hemisphere: the North Atlantic and the western North Pacific. In both regions, winter deep/intermediate waters formation favors the ocean uptake of PO. In addition, those regions are characterized by extremely thick atmospheric planetary boundary layers in winter enabling the vertical mixing of low APO surface

values up to 2000–2500 m altitude and the zonal transport by westerlies (Figure S3 in supplementary material). It is relatively certain that the PO uptake is underestimated by the models in the North Atlantic. All inverse calculations underestimate the northward heat transport in the Atlantic by about 0.2–0.6 PW compared to hydrographic section estimates of Ganachaud and Wunsch (2003) and Talley (2003) (Table 3).

The failure to duplicate the APO deficit is most certainly tied to a similar deficit in the ability of these models to duplicate independent estimates of northward heat transport. This defect could have either of two causes, i.e. it could be caused by the oceanic transports being incorrect, or it could be due to a limitation of the inverse methodology, even for realistic transports. To address this issue, we also looked at the heat transports from the MITgcm-ECCO forward model. Interhemsipheric heat transport asymmetry from the forward and inverse MITgcm-ECCO solution are the same in the Indo-pacific (−0.3 PW in Table 3) and similar in the Atlantic (0.5 and 0.6 PW in Table 3), which suggests that the inverse method is robust enough to capture large-scale meridional patterns. Despite a realistic overturning circulation (M_{North} = 20 Sv in Table 1) in agreement with observations (Talley 2008; Lumpkin and Speer 2007), the meridional heat transport in the MITgcm-ECCO forward model is in the lower range of observations in the northern hemisphere (1 PW at 20°N to be compared to observations in Fig. 7a) and lower than most observations in the southern hemisphere (−0.3 PW at 20°S to be compared to observations in Fig. 7a). However, it is difficult to investigate the details of the model biases. Where the data coverage is sufficient to capture the heat transport over a long time period, such as along the RAPID and Florida Straight surveys at 26°N (Johns et al. 2008, 2011), MITgcm-ECCO falls in the range of observed interannual variability (Table 4). MITgcm-ECCO assimilates those data; the fact that it performs well where intense data coverage is available but underestimates the heat transport asymmetry at basin- and global-scale suggests that observations are still too scarce in some regions to better constrain the ocean meridional heat transport in ocean state estimates.

The bias in the Atlantic meridional transport alone could explain most of the mismatch with APO observations. However, there is observational evidence that the sink of potential oxygen is also underestimated in the western North Pacific. Two hydrographic sections (Macdonald 1998; Talley 2003) suggest that the northward heat transport is also underestimated by ocean inversions in the North Pacific where the Kuroshio Current is located (Fig. 7c). In addition, Tohjima et al. (2012) recently presented data showing a strong surface APO deficit in the western North Pacific associated with a gradient of −15 per meg between 20°S and 40°N. This gradient in the western Pacific is more than

twice the gradient observed at the same latitude in the eastern/central Pacific (Fig. 2a). This enhanced western Pacific uptake of PO, supports the existence of a stronger northward heat transport in the Pacific, absent from our inverse estimates but in agreement with some of the data-based estimates [Macdonald (1998) and Talley (2003) in Fig. 7c].

4.3 Limitations and uncertainties

Having discussed the major insights of our study, we recognize that it is subject to certain limitations and that challenges await future studies. A major limitation of the current and previous studies based on ocean interior inversions is the assumption of steady state that gives no information on the transient changes of biogeochemical and thermal air–sea fluxes, e.g. associated with natural or anthropogenic climate changes. The ocean heat content is increasing due to recent climate change at a rate of ∼5 ZJ y^{-1} (Rhein et al. 2013) with the Southern Hemisphere taking up more heat due to its larger ocean surface. Although there is no well-constrained estimate of the contribution of global warming on CO_2 and O_2 air–sea fluxes, we can estimate an upper bound of this effect as follows.

Assuming the extreme scenario where all 5 ZJ y^{-1} enter the ocean in the Southern Hemisphere, and assuming an APO to heat ratio of 3.9 nmol J^{-1}, we find that the ocean would release 1.9×10^{13} moles of APO in the Southern hemisphere (i.e. $5 \times 10^{21} \times 3.8 \times 10^{-9}$). Assuming that the exchange time between the two hemispheres is 1 year, we find that the maximum impact of transient warming on the north-south APO gradient is ∼1.0 per meg (i.e. 1.9×10^{13} /$1.85 \times 10^{19} = 1.0 \times 10^{-6} = 1.0$ per meg, with 1.85×10^{19} being the number of moles of O_2 in one hemisphere of the atmosphere). This back of the envelope estimation corresponds to a relatively small uncertainty of ∼0.14 PW on the northward heat transport.

The steady state hypothesis of the ocean inversion also prevents us from accounting for seasonal and interannual variability in ocean circulation and hydrographic data. The framework thereby neglects co-variations between time-varying fluctuations in concentration and velocity because both are assumed constant with time. However, there is observational evidence that the meridional transport at depth varies from seasonal to interannual time scales (Johns et al. 2011; Atkinson et al. 2012).

A limitation of comparing simulated and observed atmospheric concentrations is the uncertainty in the atmospheric circulation, including uncertainties in the wind and in the atmospheric transport model. We evaluated that the uncertainty associated with the wind product is ∼0.5 per meg (Fig. 8a). The atmospheric transport model uncertainty is relevant in two contexts, the interhemispheric exchange rate of the transient anthropogenic contributions (fossil fuel

and oceanic anthropogenic CO_2 uptake) and the rectifier effect. We expect the uncertainties on the interhemispheric exchange rate to have little influence on the northern APO deficit because the well-known anthropogenic contributions, cancel each other and don't produce a large gradient in APO (Fig. 8). This situation is very different than confronted in CO_2 inversions, where the anthropogenic contributions are very large compared to the land signals of interest (Patra et al. 2011). We have tested the influence of the atmospheric transport model by comparing the northern APO deficit obtained with two transport models using a suite of observation-based air–sea fluxes (see "Appendix 3"). We find differences of the order of ∼10 % for the column-average deficit (∼0.5 per meg) and of the order of ∼ 30 % for the surface deficit (∼1.5 per meg). This supports our finding that column-average atmospheric observations provide superior constraints on air–sea exchanges on large spatial and temporal scales.

Finally, another limitation of the method is the low spatial resolution used for both the ocean inversion and the ocean models used to compute ocean transports. The ocean inversions are performed over 30 oceanic regions, which prevents us from resolving air–sea flux spatial structures at smaller scale, such as the patchiness of O_2 uptake and heat release during deep winter mixing. However, the relatively close agreement between the heat transport in the MITgcm-ECCO forward and inverse solutions (Table 3 and Sect. 4.2) suggests this effect only weakly influences the large-scale interhemispheric asymmetry.

The method can also not account for correlations on spatial scales smaller than the interior ocean model grid. Even the model with highest horizontal resolution (MITgcm-ECCO at 1° resolution) does not resolve the mesoscale, let alone the small scales on which ocean ventilation takes place. This is likely to introduce errors in the ocean mean transport (e.g., a comparison with radiocarbon data suggests that shallow-to-deep exchange is much too strong in MITgcm-ECCO; Graven et al. (2012)). Indeed, the ocean dynamics at small spatial scale influences the ocean circulation at larger scale including the shallow circulation associated with gyres, the deep meridional overturning circulation (Lévy et al. 2010; Thomas and Zhai 2013; Mazloff et al. 2013, e.g) and in turn lateral and vertical transports (Thomas and Ferrari 2008; Capet et al. 2008; Resplandy et al. 2011; Zhang et al. 2014).

5 Conclusions

The major findings of this study are:

1. On the basis of a close correlation in hydrographic data, which is supported by inverse calculations, we

find that the large-scale fluxes of potential oxygen (PO) are closely tied to heat fluxes.

2. HIPPO aircraft column-averaged data provide superior constraints on large-scale PO fluxes (compared to surface data) due to a lower sensitivity to rectifier effects and local air–sea fluxes.

3. Effects of fossil-fuel emissions and anthropogenic carbon uptake are significant, but largely cancel with relatively low uncertainty, allowing APO data to constrain pre-industrial O_2 and CO_2 fluxes.

4. APO data combined with the relationship found between PO and heat provide valuable constraints on the interhemispheric asymmetry of the oceanic heat transport (northward transport between 0.7 and 1.1 PW).

5. The constraints on heat transports obtained with APO converge with independent heat flux estimates from bulk formulations (Large and Yeager 2009) and are in the upper range of hydrographic estimates (Ganachaud and Wunsch 2003).

6. APO has the potential to be a more precise large-scale constraint, thus narrowing the uncertainty range of the heat transport asymmetry estimates based on hydrographic data.

Appendix 1: Atmospheric aircraft observations: interpolation and uncertainties

The HIPPO campaign took place between January 2009 and September 2011 aboard the National Center for Atmospheric Research/National Science Foundations Gulfstream V research jet HIAPER and mapped the vertical and meridional distribution of atmospheric carbon cycle gases and other anthropogenic tracers including CO_2 and O_2/N_2 (Wofsy 2011). We used 7 of the 10 transects performed during the five HIPPO campaigns. These transects sample a

Table 5 The 7 HIPPO transects used to construct the annual mean meridional transect

HIPPO campaign	Date	Research Flights (RF)
1	Jan. 2009	RF03–RF07
3	Mar. 2010	RF02–RF06
3	Apr. 2010	RF07–RF10
4	Jun. 2011	RF02–RF06
5	Aug. 2011	RF05–RF09
5	Sep. 2011	RF10–RF13
2	Nov. 2009	RF02–RF06

similar Pacific section between 80°N and 58°S and cover the seasonal cycle 1–2 months apart (Fig. 2; Table 5). Atmospheric O_2/N_2 was measured in-situ by the NCAR Atmospheric Oxygen Instrument and on whole air samples collected by the NCAR/Scripps Medusa flask sampler (Bent 2014). The data file we have used is that of Wofsy et al. (2012) (*HIPPO_all_missions_merge_10s_20121129.tbl*), but with an updated version of the APO data. The APO data in the 20121129 file included an adjustment of the flask data for thermal fractionation that used the measured Ar/N_2 ratios. This adjustment also affected the in situ data which are adjusted to agree with the flasks. To avoid interhemispheric gradients in Ar/N_2 affecting our results, we have used a version of the APO data without this adjustment, and will include this version of the data in an upcoming update to the official HIPPO data repository. Three transects were removed because they sampled different longitudes. APO was computed similarly to surface stations based on CO_2 concentrations and O_2/N_2 ratios at each data point (see Eq. 2). APO values were interpolated in space along this transect with a 5° longitude resolution and 19 vertical levels corresponding to the grid of the atmospheric transport model TM3 used in this study (see Sect. 8). We used a kriging interpolation method that computes the gaussian-weighted average based on the spatial covariance between triangulated data points, with a weighting radius spanning over 10° of latitude on the horizontal and 50 mb on the vertical.

We computed the northern APO deficit using data interpolated to ~900 mb (noted ΔAPO surface), which can be compared to the deficit derived from surface stations (Sect. 2.1) and data vertically integrated over the troposphere between the surface and 400 mb (noted ΔAPO troposphere). The northern deficit was estimated using the 7 HIPPO transects and a bi-harmonic seasonal fit with periods of 1 year and 6 months after de-trending and referencing the data to year 2009 using the time-series at the Cape Grim surface station. Annual mean values of the surface and tropospheric deficit were computed from these seasonal fits.

The uncertainty on the annual mean includes the impact of spatio-temporal sparsity in the data. The uncertainty on ΔAPO related to interannual variability (ϵ_{IA}) was computed using a forward predictive model with an autoregressive process of order 2 (AR2). The predictive model was used to generate a 1500-year long time-series with the same mean and variance as the data. It quantifies the error made by estimating the mean from a temporally varying 3-year long time-series. It is computed as the standard deviation between the 500 means (1500/3) estimated from 3-year long segments and the mean estimated from the 1500-year long time-series. At the surface, ϵ_{IA} = ± 1.2 per meg. Integrated over the troposphere, ϵ_{IA} is assumed to be 60 % of the uncertainty at the surface. This estimate is based on the results of the atmospheric model TM3, in which the interannual variability of the northern deficit integrated vertically and meridionally is almost half of the one obtained at the surface. The uncertainty on ΔAPO related to the spatio-temporal undersampling of the seasonal cycle ϵ_{SEAS} is estimated by sub-sampling the APO distribution obtained with the atmospheric transport model TM3 at the time and place of HIPPO transects. ϵ_{SEAS}, computed as ± the difference between the "true" mean and the mean estimated by sub-sampling, is 0.4 per meg at the surface and 0.2 per meg when integrated over the troposphere.

Appendix 2: Ocean interior inversions: computation of carbon, oxygen, nitrogen and heat air–sea fluxes

The atmospheric data are used to evaluate the fluxes of O_2, CO_2, N_2 and heat from a suite of ocean inverse calculations, which we perform based on the method of Gloor et al. (2001), Gruber et al. (2001) and Mikaloff Fletcher
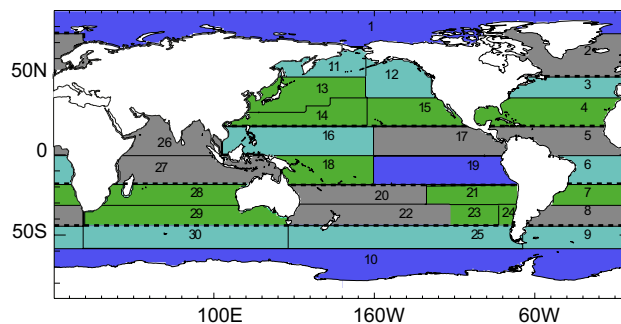

Fig. 11 Maps of 30 regions used for the ocean interior inversions (1–30 separated by thin lines) and 21 regions after aggregation of adjacent regions within individual basins (*colored*). *Thick dashed lines* indicate the large regions used to compare inverse fluxes on Fig. 4

et al. (2007). These inverse calculations rely on ocean interior data from the GLobal Ocean Data Analysis Project (GLODAP) version 1 (Key et al. 2004). Ocean interior heat was computed from GLODAP potential temperature and the sea water capacity of Millero et al. (1973). N_2 concentrations, not available in the database, were computed following Hamme and Emerson (2004) using temperature (T) and salinity (S):

$$
\begin{aligned}
ln[N_2] &= A_0 + A_1 * Ts + A_2 * Ts^2 + A_3 * Ts^3 \\
&\quad + S * (B_0 + B_1 * Ts + B_2 * Ts^2) \\
Ts &= ln\left(\frac{298. - T}{273.15 + T}\right)
\end{aligned} \tag{10}
$$

with $A_0 = 6.42931$, $A_1 = 2.92704$, $A_2 = 4.32531$, $A_3 = 4.69149$, $B_0 = -7.44129.10^{-3}$, $B_1 = -8.02566.10^{-3}$ and $B_2 = -1.46775.10^{-2}$.

The inverse method relates interior tracer fields to air–sea fluxes using steady-state basis functions computed

Table 6 Comparison to previous ocean interior inversion studies

	Fluxes	Ocean models	Inversion regions	Inversion details
Gruber et al. (2001)	O_2, N_2	MOM-LL	15(13)	2 estimates: unconstrained and constrained 0 flux
Gloor et al. (2003)	CO_2	MOM-LL	13	unconstrained
Mikaloff Fletcher et al. (2006, 2007)	CO_2	10 models including MOM-LL MOM-HH, MOM-LHS, MOM-PSS MOM-RDS, MITgcm-2.8, MITgcm-ECCO	30(24)	unconstrained
(Gerber and Joos (2010))	CO_2	Bern3D	17(16)	32 members ensemble
This study	CO_2, O_2 and N_2	MOM-LL, MOM-HH, MOM-LHS MOM-PSS, MOM-RDS MITgcm-2.8, MITgcm-ECCO	30(21)	constrained 0 flux

The number of regions used to perform the inversion (Inversion regions) and if different the number of regions retained after aggregation (*in parenthesis*)

by releasing unit dye tracer at the surface of 30 oceanic regions in a ocean general circulation model (OGCM) (Mikaloff Fletcher et al. 2006) (Fig. 11). The basis function or footprint A_i obtained for region i essentially gives the contribution of the air–sea flux of each surface region i to the concentration at each point in the ocean interior. The observed concentration is decomposed into contributions from each of the 30 regional sources:

$$C_{obs} = \sum_{i=1}^{30} \lambda_i A_i + \epsilon \qquad (11)$$

with λ_i a dimensionless factor that scales the surface unit flux and ϵ the residual concentration that can not be explained by the method. Runs were carried out for 3000 years for each models, to achieve steady state and derive the basis functions A_i. λ_i were obtained by minimizing the difference between C_{obs} and the right hand side of equation 11 using single value decomposition (see details in, Gloor et al. 2001). Regional fluxes are then given by $F_i = \lambda_i \phi_i$, with ϕ_i the rigid flux pattern specified within each surface region of the OGCM to compute the basis function. We used the spatial pattern of Takahashi et al.

Table 7 Regional air–sea heat fluxes obtained with the 7 ocean interior inversions (in PW)

Regions	MOM-HH	MOM-LHS	MOM-LL	MOM-PSS	MOM-RDS	MITgcm-2.8	MITgcm-ECCO
High Lat N 49°N/70°N:90°N							
Arctic Ocean (1)	0.04	0.09	0.09	0.13	0.09	−0.12	−0.02
North Atlantic >49°N (2)	0.35	0.25	0.27	0.20	0.24	0.70	0.78
Mid Lat N 20°N:49°N/70°N							
North Atlantic <49°N							
(3)	0.33	0.33	0.32	0.32	0.35	0.29	0.00
(4)	0.05	0.09	0.10	0.09	0.08	−0.02	0.01
North Pacific <70°N							
(11)	0.08	0.02	0.02	0.07	0.04	0.05	0.02
(12)	−0.03	−0.07	−0.08	−0.01	−0.04	0.02	−0.01
(13–14–15)	0.65	0.50	0.50	0.50	0.53	0.45	0.38
Tropics 20°S:20°N							
Atlantic							
(5)	−0.11	−0.01	−0.02	−0.08	−0.07	−0.19	0.01
(6)	−0.51	−0.46	−0.46	−0.43	−0.47	−0.44	−0.35
Pacific							
(16)	−0.12	0.16	0.16	0.07	0.11	−0.28	−0.18
(17)	−0.60	−0.29	−0.29	−0.58	−0.42	−0.59	−0.38
(18)	−0.18	0.00	−0.00	−0.07	−0.08	−0.13	−0.02
(19)	−1.16	−1.06	−1.07	−0.62	−1.06	−0.53	−0.52
Indian							
(26−27)	−0.62	−0.45	−0.45	−0.31	−0.54	−0.54	−0.47
Mid Lat S 44°S:20°S							
South Atlantic							
(7)	0.01	0.03	0.03	−0.01	0.03	0.03	−0.21
(8)	−0.29	−0.29	−0.31	−0.23	−0.29	−0.17	0.22
South Pacific							
(20−22)	0.68	0.41	0.39	0.39	0.44	0.47	0.22
(21−23−24)	−0.22	−0.26	−0.26	−0.45	−0.25	−0.24	−0.32
South Indian							
(28−29)	0.56	0.59	0.56	0.19	0.67	0.71	0.30
High Lat S < 44°S							
Subpolar < 44°S (9−25−30)	0.61	0.08	0.18	0.09	0.14	0.41	0.06
Southern Ocean < 58°S (10)	0.47	0.35	0.28	0.71	0.47	0.10	0.45

Region numbers in parenthesis refer to Fig. 11. Positive fluxes are towards the atmosphere

(2002) for CO_2 fluxes and the heat flux pattern of Esbensen and Kushnir (1981) for heat, O_2 and N_2 fluxes.

Basis functions (A_i) for the MOM models are identical to those used by Jacobson et al. (2007). The MITgcm-2.8 and MITgcm-ECCO basis functions were computed using the Transport Matrix Method (TMM), a numerical scheme for fast, "offline" simulation of passive tracers using circulations derived from ocean general circulation models as sparse "transport matrices" (TMs) (Khatiwala et al. 2005; Khatiwala 2007). For MITgcm-2.8, monthly mean TMs from an equilibrium run of the model were used to compute the basis functions, whereas for MITgcm-ECCO, monthly mean TMs representing a climatology over the 1992–2004

assimilation period were used. The TMM code and transport matrices used for these simulations are freely available from github.com/samarkhatiwala/tmm.

air–sea fluxes were estimated for the 30 regions but the result usually displayed large covariance between adjacent regions (e.g. regions 13 to 15 in the North Pacific or regions 9, 25 and 30 in the subpolar Southern Ocean) showing that these fluxes estimates are not independent. To avoid this type of underdetermination, we aggregated the 30 original fluxes into 21 regional fluxes (Fig. 11). Differences between the method used in this study and previous studies are highlighted in Table 6. Results for those 21 regions are detailed in Tables 7, 8, 9 and 10. We performed a first set

Table 8 Regional air–sea O_2 fluxes obtained with the 7 ocean interior inversions (in Tmol year^{-1})

Regions	MOM-HH	MOM-LHS	MOM-LL	MOM-PSS	MOM-RDS	MITgcm-2.8	MITgcm-ECCO
High Lat N 49°N/70°N:90°N							
Arctic Ocean (1)	3.40	−5.60	−6.78	−7.57	−3.77	16.68	9.13
North Atlantic > 49°N (2)	−41.69	−32.0262	−41.61	−20.71	−29.09	−91.66	−95.12
Mid Lat N 20°N:49°N/70°N							
North Atlantic <49°N							
(3)	−38.62	−33.20	−33.16	−28.25	−37.45	3.46	10.63
(4)	28.18	16.90	16.60	13.09	19.32	3.60	6.80
North Pacific <70°N							
(11)	−18.27	−5.15	−5.11	−16.13	−10.64	−9.41	−9.40
(12)	0.39	13.16	13.46	−4.99	3.44	−10.34	−5.17
(13–14–15)	−24.83	−33.28	−34.30	−21.84	−25.98	−15.73	−18.05
Tropics 20°S:20°N							
Atlantic							
(5)	7.64	−0.46	−0.32	6.82	4.88	18.29	13.63
(6)	46.78	37.53	38.59	35.92	41.03	48.09	23.07
Pacific							
(16)	18.31	−11.15	−12.18	5.11	−3.99	29.09	20.02
(17)	50.62	18.91	19.40	45.27	32.48	55.52	29.90
(18)	12.54	−1.71	−0.96	2.11	5.68	10.30	13.10
(19)	85.72	72.26	72.44	39.10	73.53	40.31	43.15
Indian							
(26-27)	44.89	31.66	32.07	15.30	39.38	46.37	34.17
Mid Lat S 44°S:20°S							
South Atlantic							
(7)	4.89	−0.72	−2.34	2.60	−1.59	−2.18	19.77
(8)	64.07	60.55	68.79	55.02	64.58	42.49	4.41
South Pacific							
(20−22)	−20.59	−1.46	0.52	8.50	−2.50	−20.21	10.49
(21−23−24)	33.40	37.86	35.94	57.99	41.82	28.51	40.48
South Indian							
(28−29)	−17.79	−21.18	−14.44	37.19	−32.58	−40.33	18.09
High Lat S < 44°S							
Subpolar < 44°S (9−25−30)	−168.07	−60.61	−69.54	−95.09	−95.52	−134.95	−74.20
Southern Ocean < 58°S (10)	−68.95	−80.45	−74.72	−127.45	−81.00	−16.53	−94.02

Region numbers in parenthesis refer to Fig. 11. Positive fluxes are towards the atmosphere

of inversions without constraining the balance of the total flux. We found that this method resulted in only relatively small imbalances in the predicted fluxes (for example −0.1 to 0.1 PgC y^{-1} for CO_{2pi} and 30–50 Tmol year^{-1} for O_2), which gives us confidence that this technique is able to capture large scale regional gradients.

Ocean interior inversions incorrectly interpret the addition of carbon by rivers as an air-to-sea flux (see discussion in Gruber et al. (2009) supplementary material).

At steady-state, the sum of air–sea flux and river input at global scale and hence the result of our inversion has to be balanced. We therefore performed a second set of inversions using Lagrangian multipliers to enforce the constraint that the sum of global fluxes was zero (Gloor et al. 2001). Only this second set is reported here.

Biogeochemical variables are sampled with lower coverage than temperature and salinity in the GLODAP dataset.

Table 9 Regional air–sea N_2 fluxes obtained with the 7 ocean interior inversions (in Tmol year^{-1})

Regions	MOM-HH	MOM-LHS	MOM-LL	MOM-PSS	MOM-RDS	MITgcm-2.8	MITgcm-ECCO
High Lat N 49°N/70°N:90°N							
Arctic Ocean (1)	−3.48	−7.11	−7.49	−10.49	−6.96	9.26	−0.76
North Atlantic > 49°N (2)	−27.35	−20.19	−22.76	−16.29	−19.26	−56.77	−56.48
Mid Lat N 20°N:49°N/70°N							
North Atlantic < 49°N							
(3)	−18.38	−18.66	−18.06	−16.89	−20.04	−11.08	1.59
(4)	1.62	−2.21	−2.53	−3.24	−1.35	1.87	1.31
North Pacific < 70°N							
(11)	−7.00	−2.03	−2.04	−6.41	−4.10	−4.44	−3.91
(12)	1.13	5.22	5.30	−0.61	1.89	−3.14	−0.46
(13−14−15)	−27.69	−24.47	−24.86	−22.80	−24.19	−20.25	−15.86
Tropics 20°S:20°N							
Atlantic							
(5)	5.50	0.30	0.62	4.12	3.35	10.41	0.34
(6)	29.38	24.49	24.69	23.42	25.99	26.03	19.32
Pacific							
(16)	7.83	−8.45	−8.66	−3.56	−4.98	18.18	11.98
(17)	33.52	14.45	14.56	32.06	22.81	35.42	21.92
(18)	8.32	−1.36	−1.01	2.93	3.15	5.30	−0.65
(19)	64.35	56.51	56.67	31.05	56.87	29.16	29.20
Indian							
(26−27)	36.54	23.79	23.95	16.83	29.98	31.08	25.00
Mid Lat S 44°S:20°S							
South Atlantic							
(7)	0.72	−1.46	−1.91	0.39	−1.67	−1.57	11.72
(8)	23.31	23.23	26.30	21.43	23.31	13.77	−10.41
South Pacific							
(20−22)	−32.79	−19.48	−18.31	−17.64	−20.61	−23.36	−9.07
(21−23−24)	15.63	16.72	16.51	28.77	17.16	17.21	21.51
South Indian							
(28−29)	−22.20	−24.60	−21.90	−2.66	−30.55	−31.12	−7.30
High Lat S < 44°S							
Subpolar < 44°S (9−25−30)	−41.39	2.18	−6.67	14.53	−3.27	−30.42	15.75
Southern Ocean < 58°S (10)	−46.60	−35.97	−31.33	−73.89	−46.55	−14.83	−54.40

Regions numbers in parenthesis refer to Fig. 11. Positive fluxes are towards the atmosphere

Appendix 3: Simulated atmospheric potential oxygen computation and uncertainties

To allow comparison with atmospheric data, we combined annual inverse model air–sea fluxes with additional fluxes as follows:

$$F_O = F_{Oan} + F_{Cseas} + F_{Off} \tag{12}$$

$$F_C = F_{Cpi} + F_{Cseas} + F_{Canth} + F_{Cff} \tag{13}$$

$$F_N = F_{Nan} + F_{Nseas} \tag{14}$$

The seasonal variations are those of Garcia and Keeling (2001) for O_2, Rödenbeck et al. (2013) for CO_2 and based on solubility changes expected from the seasonality of heat fluxes for N_2 (Keeling and Shertz 1992). The seasonality of O_2 was turned down by 18 % following the recent results of Bent (2014) suggesting that the amplitude reported in Garcia and Keeling (2001) was overestimated. The anthropogenic air–sea flux of CO_2 F_C^{ant} is from Khatiwala et al. (2009, 2013), the fossil fuel F_C^{ff} is taken from the Emission Database for Global Atmospheric Research (EDGAR, available at http://edgar.jrc.ec.europa.eu), and F_O^{ff} is computed by scaling F_C^{ff} using a constant stoichiometric ratio

Table 10 Regional air–sea CO_{2pi} fluxes obtained with 7 ocean interior inversions and 2009 air–sea C_{ant} fluxes from Khatiwala et al. (2009, KWLA09) (in Tmol year^{-1})

Regions	MOM-HH	MOM-LHS	MOM-LL	MOM-PSS	MOM-RDS	MITgcm-2.8	MITgcm-ECCO	C_{ant} 2009
High Lat N 49°N/70°N:90°N								
Arctic Ocean (1)	−5.13	−2.44	2.12	−7.06	−4.70	5.67	−1.54	−
North Atlantic >49°N (2)	−9.70	−9.15	−9.13	−8.91	−8.29	−22.80	−12.93	−9.17
Mid Lat N 20°N:49°N/70°N								
North Atlantic <49°N								
(3)	−12.60	−12.24	−11.87	−13.51	−12.37	−14.65	−17.58	−8.41
(4)	−5.92	−5.77	−5.94	−4.89	−5.75	−4.36	0.91	−7.95
North Pacific <70°N								
(11)	3.53	1.63	1.60	2.86	2.35	2.20	4.10	−2.43
(12)	−0.95	−3.50	−3.55	0.17	−1.72	1.45	−0.06	−4.82
(13−14−15)	−35.22	−25.00	−25.05	−29.00	−29.30	−30.05	−20.00	−14.72
Tropics 20°S:20°N								
Atlantic								
(5)	2.63	−0.04	0.28	1.58	1.02	6.08	−0.55	−3.10
(6)	15.29	14.52	14.03	13.29	14.08	11.41	7.68	−3.67
Pacific								
(16)	14.01	7.60	7.95	7.70	9.54	15.72	3.84	−5.51
(17)	5.02	5.49	5.35	12.92	5.94	4.24	1.46	−6.06
(18)	10.07	1.51	1.37	2.31	4.69	5.91	3.40	−4.32
(19)	42.00	44.30	44.33	27.96	42.16	25.92	18.76	−7.40
Indian								
(26−27)	23.33	16.67	16.59	14.98	19.69	17.30	12.08	−10.81
Mid Lat S 44°S:20°S								
South Atlantic								
(7)	−3.14	0.41	1.11	2.58	0.60	0.40	6.07	−3.76
(8)	−9.92	−12.32	−14.65	−14.40	1−4.37	−13.02	−17.95	−6.19
South Pacific								
(20−22)	−36.77	−27.80	−28.50	−30.10	−28.33	−30.56	−20.43	11.80
(21−23−24)	−5.30	−4.24	−3.59	−1.03	−7.48	1.23	4.44	−5.90
South Indian								
(28−29)	−33.71	−31.28	−32.65	31.20	−32.79	−27.53	−20.22	−15.09
High Lat S < 44°S								
Subpolar < 44°S (9-25-30)	42.68	24.15	23.95	40.96	36.18	48.66	42.81	−39.12
Southern Ocean < 58°S (10)	−0.11	17.47	16.08	12.80	8.82	−3.20	5.68	−34.24

Region numbers in parenthesis refer to Fig. 11. Positive fluxes are towards the atmosphere

of −1.4 (Keeling 1988). To enable the comparison between model estimates and airborne data, all fluxes are referenced to year 2009 by correcting for fossil fuel using EDGAR emission database and for oceanic anthropogenic carbon uptake using Khatiwala et al. (2009, 2013).

APO was estimated using Equation 8 obtained assuming there is no changes in the total moles of air and that $\left(\frac{O_2}{N_2}\right)_{reference} = \frac{X_{O2}}{X_{N2}}$ following Stephens et al. (1998). Uncertainties on resulting APO values include uncertainties on the rectifier effect, on anthropogenic carbon fluxes, on fossil fuel burning emissions and on the atmospheric circulation. The rectifier effect is the contribution to annual mean APO due to purely seasonal fluxes. We assigned a 20 % uncertainty to the seasonal rectifier effect based on the numerous studies of its dependency to both the atmospheric model used and the seasonal flux estimates (e.g., Stephens et al. 1998; Blaine 2005; Battle et al. 2006; Tohjima et al. 2012). We used the recent estimation of the uncertainty associated with fossil fuel carbon dioxide emission by Andres et al. (2014): 8.5 % (2 standard deviations). We used a conservative 20 % uncertainty on the anthropogenic air–sea flux of Khatiwala et al. (2009). The uncertainty on ΔAPO associated with the atmospheric circulation was estimated to ±0.5 per meg, by comparing APO fields obtained using NCEP winds vs. ERA-Interim winds (Fig. 8a).

Finally, we evaluated the uncertainty related to the choice of the atmospheric transport model. We compared the APO northern deficit obtained with the TM3 model and with the transport model of the Center for Climate System Research/National Institute for Environmental Studies/Frontier Research Center for Global Change (CCSR/NIES/FRCGC) (Miyazaki et al. 2008) based on EDGAR fossil fuel emissions, observation-based seasonal fluxes of O_2 (Garcia and Keeling 2001), CO_2 (Takahashi et al. 2009) and N_2 (Blaine 2005). We find that the uncertainty on the northern APO deficit is about 10 % for the column-average troposphere and about 30 % at the surface. This uncertainty is included as 1-sigma in our estimate.

References

Anderson LA, Sarmiento JL (1994) Redfield ratios of remineralization determined by nutrient data analysis. Glob Biogeochem Cycl 8(1):65–80. doi:10.1029/93GB03318

Andres R, Boden T, Higdon D (2014) A new evaluation of the uncertainty associated with CDIAC estimates of fossil fuel carbon dioxide emission. Tellus B 66(0). http://www.tellusb.net/index.php/tellusb/article/view/23616

Atkinson CP, Bryden HL, Cunningham SA, King BA (2012) Atlantic transport variability at 25°n in six hydrographic sections. Ocean Sci 8(4):497–523. doi:10.5194/os-8-497-2012

Battle M, Fletcher SM, Bender ML, Keeling RF, Manning AC, Gruber N, Tans PP, Hendricks MB, Ho DT, Simonds C, Mika R,

Paplawsky B (2006) Atmospheric potential oxygen: new observations and their implications for some atmospheric and oceanic models. Glob Biogeochem Cycl. doi:10.1029/2005GB002534

Bent J (2014) Airborne oxygen measurements over the southern ocean as an integrated constraint of seasonal biogeochemical processes. Ph.D. thesis, University of California San Diego, bluemoon.ucsd.edu/publications/jonathan/Bent_Dissertation__FINAL

Blaine TW (2005) Continuous measurements of atmospheric Ar/N_2 as a tracer of air–sea heat flux: models, methods, and data. Ph.D. Thesis, University of California, San Diego, La Jolla, 225 pp

Bryden HL, Imawaki S (2001) Ocean heat transport. In: Siedler G, Gould J (eds) Ocean circulation and climate. Academic Press, San Diego, pp 455–474

Bryden HL, King BA, McCarthy GD, McDonagh EL (2014) Impact of a 30 % reduction in Atlantic meridional overturning during 2009–2010. Ocean Sci 10(4):683–691. doi:10.5194/os-10-683-2014

Capet X, Colas F, Penven P, Marchesiello P, McWilliams JC (2008) Eastern boundary subtropical upwelling systems. In: Hecht MW, Hasumi H (eds) Eddy Resolving ocean modeling, vol 117, Geophysical Monograph Series, Washington D. C., pp 131–147

Crowley TJ (1992) North Atlantic deep water cools the southern hemisphere. Paleoceanography 7(4):489–497. doi:10.1029/92PA01058

Dee DP, Uppala SM, Simmons AJ, Berrisford P, Poli P, Kobayashi S, Andrae U, Balmaseda MA, Balsamo G, Bauer P, Bechtold P, Beljaars ACM, van de Berg L, Bidlot J, Bormann N, Delsol C, Dragani R, Fuentes M, Geer AJ, Haimberger L, Healy SB, Hersbach H, Hólm EV, Isaksen L, Kallberg P, Khler M, Matricardi M, McNally AP, Monge-Sanz BM, Morcrette JJ, Park BK, Peubey C, de Rosnay P, Tavolato C, Thpaut JN, Vitart F (2011) The ERA-interim reanalysis: configuration and performance of the data assimilation system. Q J R Met Soc 137(656):553–597. doi:10.1002/qj.828

Esbensen SK, Kushnir Y (1981) The heat budget of the global ocean: an atlas based on estimates from surface marine observations. In: Climate Res. Inst. Rep., vol 29, Oregon State Univ., USA, 27pp

Fasullo JT, Trenberth KE (2008) The annual cycle of the energy budget. Part I: global mean and landocean exchanges. J Clim 21:2297–2312. doi:10.1175/2007JCLI1935.1

Flato G, Marotzke J, Abiodun B, Braconnot P, Chou SC, Collins W, Cox P, Driouech F, Emori S, Eyring V, Forest C, Gleckler P, Guilyardi E, Jakob C, Kattsov V, Reason C, Rummukainen M (2013) Evaluation of climate models. In: Stocker TF, Qin D, Plattner GK, Tignor M, Allen SK, Boschung J, Nauels A, Xia Y, Bex V, Midgley PM (eds) Climate change 2013: the physical science basis. Contribution of working group I to the fifth assessment report of the intergovernmental panel on climate change. Cambridge University Press, Cambridge

Fuckar NS, Xie SP, Farneti R, Maroon EA, Frierson DMW (2013) Influence of the extratropical ocean circulation on the intertropical convergence zone in an idealized coupled general circulation model. J Clim 26:4612–4629. doi:10.1175/JCLI-D-12-00294.1

Ganachaud A, Wunsch C (2003) Large-scale ocean heat and freshwater transports during the world ocean circulation experiment. J Clim 16:31155–31166. doi:10.1175/1520-0442(2003)016<0696:LSOHAF>2.0.CO;2

Garcia HE, Keeling RF (2001) On the global oxygen anomaly and air–sea flux. J Geophys Res 106(C12):31,155–31,166. doi:10.1029/1999JC000200

Gerber M, Joos F (2010) Carbon sources and sinks from an ensemble kalman filter ocean data assimilation. Glob Biogeochem Cycl. doi:10.1029/2009GB003531d

Gloor M, Gruber N, Hughes TMC, Sarmiento JL (2001) Estimating net air–sea fluxes from ocean bulk data: methodology and

application to the heat cycle. Glob Biogeochem Cycl 15(4):767–782. doi:10.1029/2000GB001301

Gloor M, Gruber N, Sarmiento J, Sabine CL, Feely RA, Rödenbeck C (2003) A first estimate of present and preindustrial air–sea CO_2 flux patterns based on ocean interior carbon measurements and models. Geophys Res Lett 30(1):10-1–10-4. doi:10.1029/2002GL015594

Gnanadesikan A (1999) A simple predictive model for the structure of the oceanic pycnocline. Science 283(5410):2077–2079. doi:10.1126/science.283.5410.2077

Gnanadesikan A, Slater RD, Gruber N, Sarmiento JL (2002) Oceanic vertical exchange and new production: a comparison between models and observations. Deep Sea Res Part II Topical Stud Oceanogr 49(13):363–401. doi:10.1016/S0967-0645(01)00107-2

Graven HD, Gruber N, Key R, Khatiwala S, Giraud X (2012) Changing controls on oceanic radiocarbon: New insights on shallow-to-deep ocean exchange and anthropogenic CO_2 uptake. J Geophys Res. doi:10.1029/2012JC008074

Gruber N, Sarmiento JL (2002) Biogeochemical/physical interactions in elemental cycles. In: Robinson AR, McCarthy JJ, Rothschild BJ (eds) The Sea: biological-physical interactions in the oceans, vol 12. Wiley, New York, pp 337–399

Gruber N, Gloor M, Fan SM, Sarmiento JL (2001) Air–sea flux of oxygen estimated from bulk data: implications for the marine and atmospheric oxygen cycles. Glob Biogeochem Cycl 15(4):783–803. doi:10.1029/2000GB001302

Gruber N, Gloor M, Fletcher SEM, Doney SC, Dutkiewicz S, Follows MJ, Gerber M, Jacobson AR, Joos F, Lindsay K, Menemenlis D, Mouchet A, Müller SA, Sarmiento JL, Takahashi T (2009) Oceanic sources, sinks, and transport of atmospheric CO_2. Glob Biogeochem Cycl. doi:10.1029/2008GB003349

Hall MM, Bryden HL (1982) Direct estimates and mechanisms of ocean heat transport. Deep Sea Res 29A(3):339–359. doi:10.1016/0198-0149(82)90099-1

Ham YG, Kug JS (2012) How well do current climate models simulate two types of El Nino? Clim Dyn 39(1–2):383–398. doi:10.1007/s00382-011-1157-3

Hamme RC, Emerson SR (2004) The solubility of neon, nitrogen and argon in distilled water and seawater. Deep Sea Res Part I Oceanogr Res Pap 51(11):1517–1528. doi:10.1016/j.dsr.2004.06.009, http://www.sciencedirect.com/science/article/pii/S0967063704001190

Heimann M, Körner S (2003) The global atmospheric tracer model TM3. In: Biogeochemie MPIF (ed) Technical Report, vol 5. Max-Planck-Institut für Biogeochemie, Jena, p 131

Jacobson AR, Mikaloff Fletcher SE, Gruber N, Sarmiento JL, Gloor M (2007) A joint atmosphere-ocean inversion for surface fluxes of carbon dioxide: 2 regional resuts. Glob Biogeochem Cycl. doi:10.1029/2006GB002703

Johns WE, Beal LM, Baringer MO, Molina JR, Cunningham SA, Kanzow T, Rayner D (2008) Variability of shallow and deep western boundary currents off the Bahamas during 2004-05: results from the 26N RAPIDMOC array. J Phys Oceanogr 38(3):605–623. doi:10.1175/2007JPO3791.1

Johns WE, Baringer MO, Beal LM, Cunningham SA, Kanzow T, Bryden HL, Hirschi JJM, Marotzke J, Meinen CS, Shaw B, Curry R (2011) Continuous, array-based estimates of atlantic ocean heat transport at 26.5°n. J Clim 24:2429–2449. doi:10.1175/2010JCLI3997.1

Kalnay E, Kanamitsu M, Kistler R, Collins W, Deaven D, Gandin L, Iredell M, Saha S, White G, Woollen J, Zhu Y, Leetmaa A, Reynolds R, Chelliah M, Ebisuzaki W, Higgins W, Janowiak J, Mo KC, Ropelewski C, Wang J, Jenne R, Joseph D (1996) The ncep/ncar 40-year reanalysis project. Bull Am Met Soc 77:437–471 10.1175/1520-0477

Keeling R, Manning A (2014) 5.15 - studies of recent changes in atmospheric O_2 content. In: Holland HD, Turekian KK (eds)

Treatise on Geochemistry (Second Edition), second edition edn, Elsevier, Oxford, pp 385–404. doi:10.1016/B978-0-08-095975-7.00420-4, http://www.sciencedirect.com/science/article/pii/B9780080959757004204

Keeling RF (1988) Measuring correlations between atmospheric oxygen and carbon dioxide mole fractions: a preliminary study in urban air. J Atmos Chem 7:153–176

Keeling RF, Garcia HE (2002) The change in oceanic O_2 inventory associated with recent global warming. In: Proceedings of the National Academy of Sciences 99(12):7848–7853. doi:10.1073/pnas.122154899, http://www.pnas.org/content/99/12/7848.abstract, http://www.pnas.org/content/99/12/7848.full+html

Keeling RF, Shertz SR (1992) Seasonal and interannual variations in atmospheric oxygen and implications for the global carbon cycle. Nature 358(6389):723–727. doi:10.1038/358723a0, http://www.nature.com/nature/journal/v358/n6389/abs/358723a0.html

Keeling RF, Körtzinger A, Gruber N (2010) Ocean deoxygenation in a warming world. Annu Rev Mar Sci 2(1):199–229. doi:10.1146/annurev.marine.010908.163855

Key RM, Kozyr A, Sabine CL, Lee K, Wanninkhof R, Bullister JL, Feely RA, Millero FJ, Mordy C, Peng TH (2004) A global ocean carbon climatology: Results from Global Data Analysis Project (GLODAP). Glob Biogeochem Cycl. doi:10.1029/2004GB002247

Khatiwala S (2007) A computational framework for simulation of biogeochemical tracers in the ocean. Glob Biogeochem Cycl. doi:10.1029/2007GB002923

Khatiwala S, Visbeck M, Cane MA (2005) Accelerated simulation of passive tracers in ocean circulation models. Ocean Model 9(1):51–69. doi:10.1016/j.ocemod.2004.04.002, http://www.sciencedirect.com/science/article/pii/S1463500304000307

Khatiwala S, Primeau F, Hall T (2009) Reconstruction of the history of anthropogenic CO_2 concentrations in the ocean. Nature 462:346–349. doi:10.1038/nature08526

Khatiwala S, Tanhua T, Mikaloff Fletcher S, Gerber M, Doney SC, Graven HD, Gruber N, McKinley GA, Murata A, Ríos AF, Sabine CL (2013) Global ocean storage of anthropogenic carbon. Biogeosciences 10(4):2169–2191. doi:10.5194/bg-10-2169-2013

Large WG, Yeager SG (2009) The global climatology of an interannually varying air–sea flux data set. Clim Dyn 33(2–3):341–364. doi:10.1007/s00382-008-0441-3

Lévy M, Klein P, Tréguier AM, Iovino D, Madec G, Masson S, Takahashi K (2010) Modifications of gyre circulation by sub-mesoscale physics. Ocean Model 34:1–15. doi:10.1016/j.ocemod.2010.04.001

Li G, Xie SP (2014) Tropical biases in cmip5 multimodel ensemble: the excessive equatorial pacific cold tongue and double itcz problems. J Clim 27:1765–1780. doi:10.1175/JCLI-D-13-00337.1

Lumpkin R, Speer K (2007) Global ocean meridional overturning. J Phys Oceanogr 37:2550–2562. doi:10.1175/JPO3130.1

Macdonald AM (1998) The global ocean circulation: a hydrographic estimate and regional analysis. Prog Oceanogr 41(3):281–382. doi:10.1016/S0079-6611(98)00020-2

Mahlstein I, Knutti R (2011) Ocean heat transport as a cause for model uncertainty in projected arctic warming. J Clim 24:1451–1460. doi:10.1175/2010JCLI3713.1

Marshall J, Adcroft A, Hill C, Perelman L, Heisey C (1997) A finite-volume, incompressible navier stokes model for studies of the ocean on parallel computers. J Geophys Res Oceans 102(C3):5753–5766. doi:10.1029/96JC02775

Marshall J, Donohoe A, Ferreira D, McGee D (2014) The oceans role in setting the mean position of the inter-tropical convergence zone. Clim Dyn 42(7–8):1967–1979. doi:10.1007/s00382-013-1767-z

Mazloff MR, Ferrari R, Schneider T (2013) The force balance of the southern ocean meridional overturning circulation. J Phys Oceanogr 43:1193–1208. doi:10.1038/ngeo1193

Mikaloff Fletcher SE, Gruber N, Jacobson AR, Doney SC, Dutkiewicz S, Gerber M, Follows M, Joos F, Lindsay K, Menemenlis D, Mouchet A, Mueller SA, Sarmiento JL (2006) Inverse estimates of anthropogenic CO_2 uptake, transport, and storage by the ocean. Glob Biogeochem Cycl 20(2). doi:10.1029/2005GB002530, http://dx.doi.org/10.1029/2005GB002530

Mikaloff Fletcher SE, Gruber N, Jacobson AR, Gloor M, Doney SC, Dutkiewicz S, Gerber M, Follows M, Joos F, Lindsay K, Menemenlis D, Mouchet A, Müller SA, Sarmiento JL (2007) Inverse estimates of the oceanic sources and sinks of natural CO_2 and the implied oceanic carbon transport. Glob Biogeochem Cycl 21(1). doi:10.1029/2006GB002751, http://dx.doi.org/10.1029/2006GB002751

Millero FJ, Perron G, Desnoyers JE (1973) Heat capacity of seawater solutions from 5° to 35°c and 0.5 to 22 permil chlorinity. J Geophys Res 78(21):4499–4507. doi:10.1029/JC078i021p04499

Miyazaki K, Patra PK, Takigawa M, Iwasaki T, Nakazawa T (2008) Global-scale transport of carbon dioxide in the troposphere. J Geophys Res Atmos 113(D15):D15,301. doi:10.1029/2007JD009557

Nevison CD, Mahowald NM, Doney SC, Lima ID, Cassar N (2008) Impact of variable air–sea o_2 and co_2 fluxes on atmospheric potential oxygen (apo) and land-ocean carbon sink partitioning. Biogeosciences 5(3):875–889. doi:10.5194/bg-5-875-2008

Palter JB, Sarmiento JL, Gnanadesikan A, Simeon J, Slater RD (2010) Fueling export production: nutrient return pathways from the deep ocean and their dependence on the meridional overturning circulation. Biogeosciences 7(11):3549–3568. doi:10.5194/bg-7-3549-2010

Patra P, Houweling KS, Krol M, Bousquet P, Belikov D, Bergmann D, Bian H, Cameron-Smith P, Chipperfield MP, Corbin K (2011) Transcom model simulations of ch_4 and related species: linking transport, surface flux and chemical loss with ch_4 variability in the troposphere and lower stratosphere. Atmos Chem Phys 11(24):12,813–12,837

Philander SGH, Gu D, Lambert G, Li T, Halpern D, Lau NC, Pacanowski RC (1996) Why the ITCZ is mostly north of the equator. J Clim 9(5):2958–2972. doi:10.1175/1520-0442(1996)009<2958:WTIIMN>2.0.CO;2

Resplandy L, Lévy M, Madec G, Pous S, Aumont O, Kumar D (2011) Contribution of mesoscale processes to nutrient budgets in the Arabian Sea. J Geophys Res. doi:10.1029/2011JC007006

Rhein M, Rintoul SR, Aoki S, Campos E, Chambers D, Feely RA, Gulev S, Johnson GC, Josey SA, Kostianoy A, Mauritzen C, Roemmich D, Talley LD, Wang F (2013) Observations: Ocean. In: Stocker TF, Qin D, Plattner GK, Tignor M, Allen SK, Boschung J, Nauels A, Xia Y, Bex V, Midgley PM (eds) Climate change 2013: the physical science basis contribution of working group i to the fifth assessment report of the intergovernmental panel on climate change. Cambridge University Press, Cambridge

Rödenbeck C, Keeling RF, Bakker DCE, Metzl N, Olsen A, Sabine C, Heimann M (2013) Global surface-ocean pCO_2 and sea-air CO_2 flux variability from an observation-driven ocean mixed-layer scheme. Ocean Sci 9(2):193–216. doi:10.5194/os-9-193-2013

Schneider T, Bischoff T, Haug GH (2014) Migrations and dynamics of the intertropical convergence zone. Nature 513:45–53. doi:10.1038/nature13636

Severinghaus JP (1995) Studies of the terrestrial o_2 and carbon cycles in sand dune gases and in biosphere 2. In: Ph.D. thesis, Columbia Univ., New York

Stephens BB, Keeling RF, Heimann M, Six KD, Murnane R, Caldeira K (1998) Testing global ocean carbon cycle models using measurements of atmospheric O_2 and CO_2 concentration. Glob Biogeochem Cycl 12(2):213–230. doi:10.1029/97GB03500

Takahashi T, Sutherland SC, Sweeney C, Poisson A, Metzl N, Tilbrook B, Bates N, Wanninkhof R, Feely RA, Sabine C, Olafsson J, Nojiri Y (2002) Global sea-air CO_2 flux based on climatological surface ocean pCO_2, and seasonal biological and temperature effects. Deep Sea Res Part II Top Stud Oceanogr 49(9–10):1601–1622. doi:10.1016/S0967-0645(02)00003-6. http://www.sciencedirect.com/science/article/B6VGC-452W7KK-2/2/cf337375806e31b8c4579d8e5d9a98c7, the Southern Ocean I: Climatic Changes in the Cycle of Carbon in the Southern Ocean

Takahashi T, Sutherland SC, Wanninkhof R, Sweeney C, Feely RA, Chipman DW, Hales B, Friederich G, Chavez F, Sabine C, Watson A, Bakker DC, Schuster U, Metzl N, Yoshikawa-Inoue H, Ishii M, Midorikawa T, Nojiri Y, Körtzinger A, Steinhoff T, Hoppema M, Olafsson J, Arnarson TS, Tilbrook B, Johannessen T, Olsen A, Bellerby R, Wong C, Delille B, Bates N, de Baar HJ (2009) Climatological mean and decadal change in surface ocean pCO_2, and net sea-air CO_2 flux over the global oceans. Deep Sea Res Part II Top Stud Oceanogr 56(8–10):554–577. doi:10.1016/j.dsr2.2008.12.009, http://www.sciencedirect.com/science/article/B6VGC-4V59VVH-1/2/6c157bd4052048ac211736c038787a3a, surface Ocean CO2 Variability and Vulnerabilities

Talley LD (2003) Shallow, intermediate, and deep overturning components of the global heat budget. J Phys Oceanogr 33(3):530–560. doi:10.1175/1520-0442(1996)009<2958:WTIIMN>2.0.CO;2

Talley LD (2008) Freshwater transport estimates and the global overturning circulation: Shallow, deep and throughflow components. Prog Oceanogr 78(4):257–303. doi:10.1016/j.pocean.2008.05.001, http://www.sciencedirect.com/science/article/pii/S0079661108001080

Thomas L, Ferrari R (2008) Friction, frontogenesis, frontal instabilities and the stratification of the ocean surface mixed layer. J Phys Oceanogr 38:2501–2518

Thomas MD, Zhai X (2013) Eddy-induced variability of the meridional overturning circulation in a model of the north atlantic. Geophys Res Lett 40(11):2742–2747. doi:10.1002/grl.50532

Tohjima Y, Mukai H, Machida T, Nojiri Y, Gloor M (2005) First measurements of the latitudinal atmospheric O_2 and CO_2 distributions across the western Pacific. Geophys Res Lett. doi:10.1029/2005GL023311

Tohjima Y, Minejima C, Mukai H, Machida T, Yamagishi H, Nojiri Y (2012) Analysis of seasonality and annual mean distribution of atmospheric potential oxygen (APO) in the Pacific region. Glob Biogeochem Cycl. doi:10.1029/2011GB004110

Trenberth KE, Caron JM (2001) Estimates of meridional atmosphere and ocean heat transports. J Clim 14:3433–3443. doi:10.1175/1520-0442(2001)014<3433:EOMAAO>2.0.CO;2

Trenberth KE, Fasullo JT (2008) An observational estimate of inferred ocean energy divergence. J Phys Oceanogr 38:984–999. doi:10.1175/2007JPO3833.1

Wofsy SC, Daube BC, Jimenez R, Kort E, Pittman JV, Park S, Commane R, Xiang B, Santoni G, Jacob D, Fisher J, Pickett-Heaps C, Wang H, Wecht K, Wang QQ, Stephens BB, Shertz S, Watt A, Romashkin P, Camposv T, Haggerty J, Cooper WA, DRogers, Beaton S, Hendershot R, Elkins JW, Fahey DW, Gao RS, Moore F, Montzka SA, Schwarz JP, Perring AE, Hurst D, Miller BR, Sweeney C, Oltmans S, Nance D, Hintsa E, Dutton G, Watts LA, Spackman JR, Rosenlof KH, Ray EA, Hall B, Zondlo MA, Diao M, Keeling R, Bent J, Atlas EL, Lueb R, Mahoney MJ (2012) Hippo merged 10-second meteorology, atmospheric chemistry, aerosol data (r_20121129). doi:10.3334/CDIAC/hippo_010, carbon Dioxide Information Analysis Center, Oak Ridge National Laboratory, Oak Ridge, Tennessee, USA

Wofsy SC et al (2011) HIAPER pole-to-pole observations (HIPPO): fine-grained, global-scale measurements of climatically

important atmospheric gases and aerosols. Philos Trans R Soc A Math Phys Eng Sci 369(1943):2073–2086. doi:10.1098/rsta.2010.0313

Wunsch C, Heimbach P, Ponte RM, Fukumori I, the ECCO-GODAE Consortium Members (2009) The global general circulation of the ocean estimated by the ecco-consortium. Oceanography. doi:10.5670/oceanog.2009.41

Zhang Z, Wang W, Qiu B (2014) Oceanic mass transport by mesoscale eddies. Science 345(6194):322–324. doi:10.1126/science.1252418